

ISP-Agnostic Image Reconstruction for Under-Display Cameras

Miao Qi Yuqi Li Wolfgang Heidrich
KAUST Visual Computing Center
Saudi Arabia

miao.qi@kaust.edu.sa

liyuqi1@nbu.edu.cn

wolfgang.heidrich@kaust.edu.sa

Abstract

Under-display cameras have been proposed in recent years as a way to reduce the form factor of mobile devices while maximizing the screen area. Unfortunately, placing the camera behind the screen results in significant image distortions, including loss of contrast, blur, noise, color shift, scattering artifacts, and reduced light sensitivity.

In this paper, we propose an image-restoration pipeline that is ISP-agnostic, i.e. it can be combined with any legacy ISP to produce a final image that matches the appearance of regular cameras using the same ISP. This is achieved with a deep learning approach that performs a RAW-to-RAW image restoration.

To obtain large quantities of real under-display camera training data with sufficient contrast and scene diversity, we furthermore develop a data capture method utilizing an HDR monitor, as well as a data augmentation method to generate suitable HDR content. The monitor data is supplemented with real-world data that has less scene diversity but allows us to achieve fine detail recovery without being limited by the monitor resolution. Together, this approach successfully restores color and contrast as well as image detail.

1. Introduction

Ever since the invention of smart phones, there has been a push to maximize the available screen area as a percentage of the total device surface area. As a result, most other components have now been removed completely from the front face of the phone, with one notable exception: the user-facing, or “selfie” camera, which is usually placed in a “notch” or hole cut out from the display.

For aesthetic and usability reasons, it has been proposed that the selfie camera could be moved under the display [22]. This concept would make use of the fact that OLED displays can be embedded in a transparent substrate. Since the actively emitting area of an OLED pixel is much smaller than the pixel spacing, sufficient light may pass

through the display to reach the camera.

Unfortunately, the commercial adoption of this concept has been relatively slow due to the degradation in image quality (see Fig. 1). Specifically, the regular pixel structures in the display act as a diffraction grating that distorts the captured image [30]. We can observe some amount of blur, a “haze”-like reduction in contrast (due to a blur kernel with a long tail), as well as significant color distortion from the absorption in the display.

Image reconstruction for this type of under-display camera (UDC) therefore entails deblurring, dehazing, color restoration, as well as handling increased noise due to the reduced amount of light incident on the camera. Although the distortion appears to be largely shift-invariant, this remains a difficult reconstruction problem.

For practical deployment, there is another major consideration: smart phone manufacturers have invested a significant amount of effort into developing image signal processing (ISP) pipelines for their products. These are complicated systems that achieve a certain brand-specific look, which we would like to preserve. One way to achieve this goal would be to attempt to train a deep network to not only perform the image reconstruction, but also emulate a given ISP at the same time. However, this approach requires that the deep network not only learns the UDC reconstruction task but also an immensely complex black-box ISP system, which would require infeasible amounts of training data (images captured with an UDC and a comparison regular camera). Instead, we opt for an ISP-agnostic design enabled by a raw-to-raw training pipeline. Please see Section 3.2 for a more detailed discussion of this design choice.

Our RAW-to-RAW reconstruction framework is based on a Wasserstein generative adversarial network with gradient penalty (WGAN-GP) deep network architecture [7], which can be successfully trained to deal with the distortions of the UDC images. We also devise a new HDR monitor-based capture setup that allows us to easily capture image pairs with a UDC camera and a regular reference camera. This setup allows us to train the network on the overall reconstruction task with a large scene diversity with

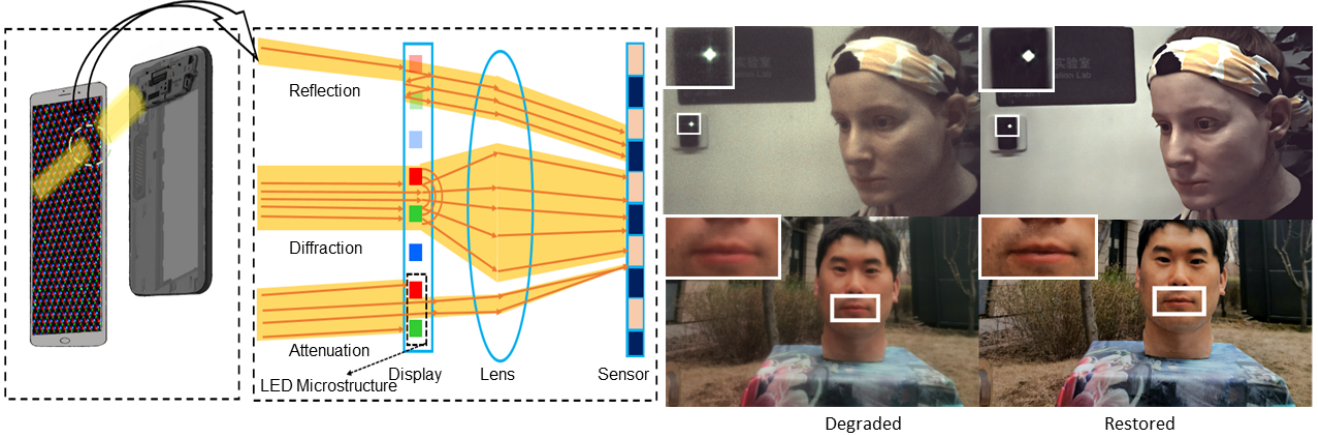


Figure 1. Under-display camera (UDC) optics and example images. The left figure is an illustration of optical distortions created by under display cameras. Three main optical effects cause image degradation in UDC cameras: a) blocking and absorption of light in the display results in brightness and color distortions. b) the regular pixel structures of the display act as a diffraction grating that haze-like low frequency blur as well as stripe artifacts around light sources. c) Multiple reflection between the display layers results in a relatively compact blur. The right figure shows the resulting image degradation as well as our restoration result. We can see all of the mentioned degradations in the right figure, especially the “stripe-like” artifact of the green spot light in the right top image. We removed it very successfully in the restored image. In the right bottom, degraded image contrast become low and the man’s mustache detail is blurred and lost in the degraded image, but all restored in our restored image.

challenging high contrast scenes that would be exceedingly difficult and cumbersome to capture “in the wild”. On the other hand, any monitor-based capture system is inherently limited by the pixel count of the display; we therefore supplement this data with a limited real-world dataset that has much reduced scene diversity but full resolution. In summary, we make the following technical contributions:

- In order to preserve the brand-specific ISP feature, we develop an ISP-agnostic RAW-to-RAW pipeline. Ours is the first work to tackle the UDC reconstruction problem in a RAW-to-RAW fashion.
- We propose a HDR data augmentation method for HDR portrait images.
- We propose a series of data collection methods and corresponding preprocessing methods to create a large dataset of high-quality under-display camera images.
- We test our algorithm on both monitor data and real-world data.

2. Related Work

Image restoration from under-display cameras is a fairly recent problem, which is only considered by a small number of peer reviewed publications so far [35]. However, the problem bears similarity to other image reconstruction tasks that have been more thoroughly researched, including dehazing, deblurring, denoising, and color correction.

Image Dehazing and Deblurring. An early example of image de-hazing was based on manually designed image priors, such as the highly successful dark channel prior [9]. More recently, the attention has shifted to deep learning approaches. DehazeNet [2] was directly inspired by the dark channel prior in their choice of the “Maxout” activation function. Li et al. [16] proposed a CNN based on the atmospheric scattering model and designed an end-to-end neural network. Chen [4] introduced dehazing CNN with a ResNet structure, featuring gated fusion with a multiscale approach, while Guo [8] utilized a dense-connection encoder-decoder network operating on each color channel independently.

Multiscale processing is very useful also in image deblurring. Nah et al. [20] proposed a multiscale deblur neural network structure and loss function. Kupyn et al. [15] introduced the DeblurGAN, which can achieve a state-of-art deblurring result.

Imaging Through Scattering Media. A closely related problem is that of imaging through scattering media, which is usually tackled with a more model-based approach, for example by measuring the transmission matrix [24]. The scattering inside optically thin media exhibits a “memory effect” [6], and within the region of this memory effect the blur kernel is shift-invariant, so that the image formation model simplifies to a convolution. At the same time, the blur kernels exhibit long tails, creating a haze-like reduction of contrast [14]. These results are directly applicable to the restoration problem for under-display cameras, since the display layer acts as a weakly scattering diffuser. This

is similar to the contrast reduction observed in recent works on diffractive optical elements [23].

Deep Learned ISPs. Recently, Ignatov [12] proposed to train a single deep network to replace legacy ISPs. While their results are promising, they also highlight the difficulties in trying to fit such large, complex software systems with single network: the authors report PSNR values only around 21 dB. The most recent results from the neural network ISP challenge [11], report PSNR values of up to 24 dB, which is still not considered sufficient for commercial deployment. This observation is one reason why we decide on an ISP-agnostic design (Sec. 3.2.)

ISP-Dependent and Monitor Data UDC Restoration

At ECCV 2020, Zhou et al. for the first time held a UDC restoration challenge, resulting in four contributions [37, 33, 27, 29]. The dataset for the challenge is captured on machine vision camera with a simulated UDC hardware. Because of the use of a machine vision camera, the dataset does not involve complicated ISP process as it would on smart phone systems, which is where real UDC hardware would likely be deployed. Instead, our dataset is based on a real smartphone camera with a UDC configuration.

Furthermore, the data from the challenge is captured exclusively on a standard dynamic range (SDR) monitor. This is problematic since many of the artifacts caused by diffraction are actually only visible in high contrast scenes and around light sources (see e.g. [25, 28]). Such imagery cannot be created on an SDR monitor. Furthermore, all monitor data is limited by the pixel resolution of the screen, as we demonstrate in this work that this limits the overall achievable reconstruction quality on real world data. In our work, we resolve these issue by combining HDR monitor data with a real-world dataset that can be used to fine-tune the recovery of small high frequency features.

Most recently, Yang et al. [32] proposed a screen design optimization for the UDC screen which improves the UDC image quality by choosing a randomized layout for the LED subpixel structures in the display. This work is orthogonal to our approach, and the two methods could easily be combined.

RAW-to-RAW Pipelines Recently, some RAW-to-RAW pipelines have been introduced for image restoration tasks such as super resolution [31, 34] and denoising [1, 3]. However, to the best of our knowledge, we are the first to tackle the UDC restoration problem in this fashion.

3. Problem Description and System Design

3.1. UDC Image Formation Model

Placing a transparent display on top of a camera degrades the image in a number of ways (compare Fig. 1). First, the display absorbs some of the light, and this absorption is wavelength-dependent. Therefore we expect both lower light sensitivity (i.e. increased noise) and color distortions. Second, the pixels of the display form a regular grid of micro-structures that act as a diffraction grating, which amounts to a chromatic blur that is mostly shift invariant except in the case of lens distortion [25, 32]. Finally, the front and back surface of the display can create multiply reflected light paths, which also result in image blurring with a shift-invariant PSF. The total model can be expressed as

$$i_k(x, y) = \int c_k(\lambda) d(\lambda) [s(x, y, \lambda) * o(x, y, \lambda)] d\lambda + n(x, y) \quad (1)$$

where $o_k(x, y)$ is channel k of the intrinsic object/scene that needs to be reconstructed

$$o_k(x, y) = \int c_k(\lambda) o(x, y, \lambda) d\lambda, \quad (2)$$

while $s_k(x, y, \lambda)$ is the corresponding full system point spread function (PSF). $c_k(\lambda)$ is the absorption coefficient of color channel k in the sensor for a given wavelength, and $d(\lambda)$ is the absorption of the OLED display. $n(x, y)$ is the system noise, while $i_k(x, y)$ is the image captured by the camera sensor. Reconstructing $o_k(x, y)$ from $i_k(x, y)$ is an ill-posed inverse problem.

Especially the diffractive part of the blur causes issues, since it can have a long “tail” due to higher diffraction orders [28], and it is also strongly wavelength-dependent, while the sensor data has only three color channels instead of full spectral information. This makes it necessary to employ deep learning image reconstruction approaches instead of older optimization-based approaches.

3.2. ISP-Agnostic Pipeline

There three main options for how image reconstruction tasks can interact with existing ISP software: first we could design an RGB-to-RGB pipeline, that takes as input an ISP processed image and outputs another RGB image that hopefully mimics the appearance of a regular, ISP-processed camera image without UDC hardware. This approach is complicated by the complexity of modern ISPs that perform scene-dependent processing (e.g. for portraits vs. landscapes, dark vs. bright environments etc.), as well as non-linear processing such as lookup tables. Because UDC image and reference training images could be processed differently by the ISP, training a network to be able to work with all different combinations of internal choices in the black-box ISP would require prohibitive amounts of training data.

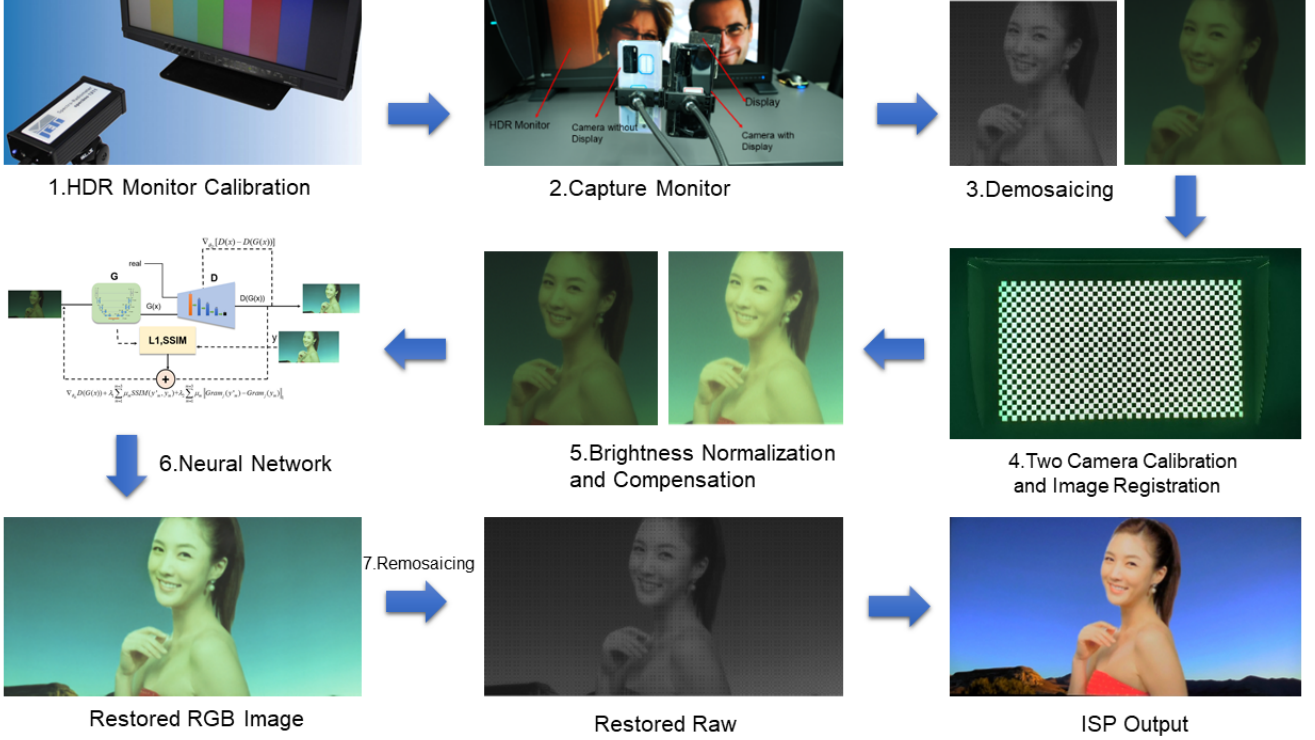


Figure 2. Our RAW-to-RAW pipeline. Our pipeline includes the following steps: 1. calibration of the HDR monitor to produce colors and intensities matching real-world scenes; 2. capture of image pairs with two smartphones (one regular camera, and one UDC camera); 3. simple interpolation-based demosaicking to get three color channels for each pixel; 4. image registration by homography; 5. brightness normalization; 6. WGAN-GP based image reconstruction; and 7. re-apply a Bayer filter pattern to convert the image back to raw format. After this pipeline, a legacy ISP can be used to obtain the final image.

A second design choice would be a RAW-to-RGB pipeline, which takes as input a raw image and produces an output that looks like an ISP processed image of a reference camera. While slightly easier than the first design choice, this approach still conflates the learning of the UDC restoration problem with the blackbox learning of the ISP module, and as discussed in Section 2, even just the latter task is difficult enough that there is currently no truly satisfactory solution.

The final design choice is to employ a RAW-to-RAW pipeline, which completely sidesteps the ISP complexities, and allows the neural network to focus exclusively on the UDC reconstruction task. After raw image restoration, any existing legacy ISP can be applied to achieve the desired look in the final image. Figure 2 shows an overview of our pipeline.

4. Network Architecture and Loss

As shown in the supplementary Fig. S2, for the neural network we choose the WGAN-GP structure [7]. This choice is motivated by a number of considerations. First, GANs excel at preserving and recovering texture detail [15], which is required in UDC cameras due to the display-

induced blur. GANs have also shown to work very well on style transfer and other image to image mappings [39], which is a task similar to the color and contrast restoration problem in UDC images. As a semi-supervised learning method, GANs also generally minimize the amount of training data needed, which is advantageous in our setting. Finally, the WGAN-GP in particular is very stable and easy to train [7].

The WGAN-GP loss can be written as:

$$\mathcal{L}_a = \mathbb{E}_{x \sim \mathbb{P}_r} [D(x)] - \mathbb{E}_{x' \sim \mathbb{P}_g} [D(x')] + \lambda_g \mathbb{E}_{x' \sim \mathbb{P}_g} [\|\nabla_{x'} D(x')\|_2 - 1], \quad (3)$$

where \mathbb{P}_r is the real image distribution, \mathbb{P}_g is the generated image distribution, and $D(x)$ represents the output of the discriminator. The last term is the gradient penalty term.

Since our training images have slight variations in the brightness mapping, we use both the SSIM loss and the perceptual loss to compare images, since SSIM is less sensitive to such differences [36]. The combined content loss is then:

$$\mathcal{L}_c = \lambda_1 SSIM(y' - y) + \lambda_2 \|Gram_j(y') - Gram_j(y)\|_1, \quad (4)$$

where y is the ground truth degraded image. y' is the restored image. λ_1 and λ_2 are the weights for the SSIM and

perceptual loss. $Gram_j$ is the Gram matrix defined by:

$$Gram_j(y) = F_j(y)F_j(y)^T / C_j H_j W_j, \quad (5)$$

and $F_j(x)$ is the VGG19 j -th layer output feature. C, H, W are of the size of the features. Here we choose the $j = 15$. In the end, the overall loss is:

$$\mathcal{L}_{total} = \mathcal{L}_a + \mathcal{L}_c, \quad (6)$$

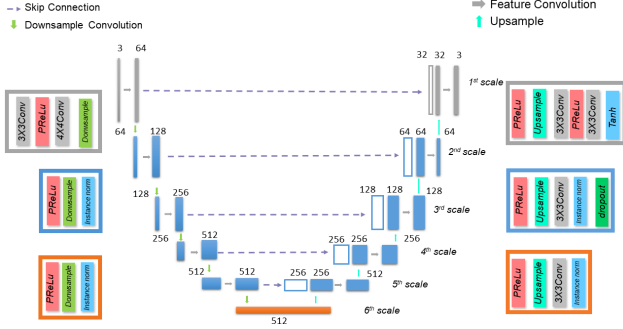


Figure 3. The generator network. The architecture was carefully tuned to the UDC problem (see text). The color outlines indicate the structure of correspondingly colored blocks in the encoder and decoder. Because the pooling layer will lose some information, we replace the pooling layer with convolution with stride of 2.

Generator The generator is an encoder-decoder structure as shown in Fig. 3. The following are the tailored improvements for our task to the generator: *a)* We replace the pooling layer with stride 2 downsample convolution layer. Because in our task, the PSF is shift-invariant, our convolution kernel does not need a large receptive field, and the pooling layer will cause some information loss. By using this downsample convolution layer, we can not only shrink the image size and match it with different scales, but also counteract the loss of information. *b)* We replace the transpose convolution with upsampling. This can avoid block artifacts (see supplement Fig. S3). *c)* In the encoder part, we use a bigger convolution kernel (4×4) to have a broader view. In the decoder part, we use the smaller convolution kernel (3×3) to preserve the fine detail. *d)* Because our training batch is small, the variance of different batches is large. Therefore, we use the instance norm.

Discriminator We use a simple CNN as a discriminator. Since the WGAN-GP architecture does not allow for the use of the batch norm, we use the instance norm instead. For the activation function, we use the LeakyReLU as suggested by Gulrajani et al. [7]. The convolution kernel is 4×4 .

5. Training Dataset

For training the network we require image pairs composed of one image from a UDC camera and one image

from a reference camera that does not have a screen in front of it, but is otherwise identical. As mentioned in the introduction, our training data is composed of two types of data: image pairs captured of an HDR monitor, and real world data.

5.1. Monitor Dataset

5.1.1 Data Collection Setup

The purpose of the monitor data is to be able to cover a large diversity of scenes such as both indoor and outdoor scenes, including those specific to a range of geographic locations. Traveling to such a variety of environments with a UDC and reference camera would be impractical. For quality training we also require excellent pixel-to-pixel alignment between the UDC and reference image, which is easily achieved with a homography on monitor data, but can be difficult for real world scenes, especially those with high depth complexity (also see Section 5.2).

The monitor capture setup is centered around an Eizo CG3145 HDR monitor with a resolution of $4,096 \times 2,160$. This monitor uses the dual modulation principle [26] to generate a typical contrast ratio of 1,000,000:1. However, unlike most dual modulation HDR monitors that use an LCD illuminated by a low-frequency LED backlight [26], the Eizo CG3145 actually uses two LCD layers stacked on top of each other on the same glass substrate. This allows the monitor to achieve not only high global contrast, but also excellent local contrast of high frequency features. This makes the monitor ideally suited for re-photography and similar tasks. Although the monitor can not achieve a *peak brightness* comparable to sunny outdoor scenes, it can achieve the *peak contrast* of the vast majority of real world environments, and as such can realistically generate glare effects due to the diffraction in the UDC setup.

5.1.2 HDR Portrait Dataset

Since UDC cameras are designed to be facing the user, selfies and group selfies and group selfies (“groufies”) are the primary type of images the camera is intended for. We took this data bias into account and generated a large amount of portrait images for display. Selfies are often taken under challenging lighting situations, with people posing in front of bright, sunlit landscapes or in dark restaurants. Our use of an HDR monitor is motivated by this observation, as well as by the realization that diffraction artifacts often show only in high contrast scenes.

Unfortunately, there is no publicly available database of HDR portrait or selfie photos with different real world backdrops. We therefore decided to create our own dataset by compositing SDR portraits into HDR background images (see the Supplement Fig. S5). To this end, we collected five thousand high-quality human half-length portraits with

masks from the public matting human dataset¹. We also collect two thousand HDR images from the HDRIHAVEN dataset. We treated the portrait and HDR images as foreground and background, respectively, and fused them to generate display images using alpha-matting. Finally, we manually selected 850 credibly looking composites to serve as content to be shown on the HDR monitor (764 for training and 86 for testing). More details as well as example images of the dataset can be found in the Supplement.

Note that a straightforward compositing of the two datasets mixes different lighting conditions for the foreground portraits and the background environments. However, this is not a concern in our setting, since such situations can also occur in real images, e.g. when photographing from a shaded region into a sunlit background. Furthermore in our RAW-to-RAW pipeline any potential scene dependent decisions of an ISP are absent so that the restoration of UDC images should be largely independent of specific scene composition. Finally, the manual screening eliminates the most unnatural looking composites.

5.2. Real World Dataset

While the monitor data provides a large diversity of scene content and illumination scenarios, its spatial resolution is limited by the 2 Mpixel resolution of the HDR display. To finetune the network training for full camera resolution, we therefore also captured a real world dataset with a much more limited diversity of scenes.

These image pairs were captured on a tripod-mounted camera with and without the UDC hardware. Overall we collected 1020 image pairs, mostly indoors. We performed automatic pixel-to-pixel alignment on all image pairs, by first extracting the image features of UDC and reference images. Based on these features, we computed the homography matrix [19] and applied it to the UDC image. In addition, we computed the optical flow between the two images and warped the reference image accordingly for a pixel-to-pixel alignment.

Although this process produces good results for scenes of moderate complexity, it does not work sufficiently well on all images. We therefore manually selected 620 images where the alignment process was considered successful (520 for fine-tuning the training and 100 for testing).

Note that automatic pixel-to-pixel image alignment tends to fail in difficult lighting situations or when the depth complexity of the scene is too high. Overall this results in a limited scene diversity in the real world dataset (indoor scenes with good illumination and not too complex object geometry). As a result, this dataset is suitable for fine-tuning but not for training the UDC reconstruction process from scratch.

¹https://github.com/aisegmentscn/matting_human_datasets

Data Augmentation		Loss Function			PSNR	SSIM
Brightness Augmentation	Resize	SSIM	L1	Perceptual Loss		
✓		✓	✓		32.23	0.76
✓	✓	✓	✓		33.76	0.88
		✓		✓	34.09	0.85
✓		✓		✓	34.22	0.88
✓	✓	✓		✓	35.72	0.92

Table 1. Data augmentation and loss function ablation study

5.3. Data Augmentation

We performed data augmentation for the training data. In addition to the standard crop, flip, transpose operations [10], we also introduced resizing and brightness augmentation. Resizing augmentation was done by resizing the degraded and ground truth image to different scale.

The brightness augmentation was done by multiplying a factor number to the pixel value of degraded and ground truth image. For details, please refer to the Supplement.

5.4. Training and Test Detail

As mentioned above, we use the monitor dataset for pre-training, to obtain a large scene diversity, and then fine-tune using the real world data. Because of the limited GPU memory, we divided the input image pairs into 512×512 tiles. The resizing augmentation was used to achieve multi-scale training. We normalized the input data to $[-1, 1]$. The Adam optimizer was used with learning rate 0.9 and weight decay 0.999. The batch size is 2. We use a lower weight for the perceptual loss and a higher one for SSIM, which is less sensitive to brightness differences. We find that $\lambda_g = 10$ in Eq. 3 and SSIM weight $\lambda_1 = 50$ and perceptual loss weight $\lambda_2 = 30$ in Eq.4 gave the best performance.

6. Experimental Results

6.1. Ablation Study

To understand the impact of our data augmentation and loss function contribution, we conduct an ablation study. We incrementally added one improvement to each case at a time. As shown in Table 1, the biggest gain comes from the resizing data augmentation. As shown in the first and second row, there is a gain of about 1.5 dB in PSNR and about 0.12 improvement in the SSIM. The reason is that we train on cropped images in order to save memory and time. However, this may make it harder for the network to learn global structures. The resizing augmentation counteracts this problem by establishing a multi-scale strategy.

The brightness augmentation is necessary because the final test image is captured in auto exposure mode and with all kind of different scenes. The brightnesses vary over a wide range. In order to test the model performance, we also include some images captured in the extreme exposure settings, including both under- and over-exposed scenes. With-

	Raw Image				ISP-proceed Image			
	PSNR	SSIM	LPIPS	CIEDE2000	PSNR	SSIM	LPIPS	CIEDE2000
Degraded Image	22.85	0.84	0.336	0.08	22.85	0.85	0.154	6.32
Restored Image	33.95	0.95	0.133	0.02	34.81	0.94	0.048	1.83

Table 2. Monitor dataset restoration results. The CIEDE2000 [18] is the average value.

out such brightness augmentation, the learning tends to result in over-fitting. See our ablation study (Table 1), rows 3 and 4. The SSIM is improved by about 0.03.

Unlike most conditional GAN papers [13] that choose the L1 loss, we choose the perceptual loss as part of the content loss. The rationale and more detail can be found in the Supplement.

In order to illustrate why we choose the RAW-to-RAW pipeline, we performed an experiment to let the neural network learn in the ISP-processed image dataset directly. The result is in the Supplement. As shown in Supplement Fig. S7, the output result is even worse than the input. This is because in our case, the difference between the degraded image and ground truth image caused by UDC is even less than the difference caused by unpaired brightness and color. The tendency is that the network tries to learn brightness and color features first. However, this change is so evident that it will also mislead the neural network to “learn” the wrong features. The brightness and color changes are so unpredictable that usually the neural network ends up not affecting the final image at all.

After the restoration, we applied a Bayer pattern to the output RGB image. This converts the restored RGB image to a raw image format again, which can then be processed by the standard cell phone ISP (or any other desired ISP). In the following we show our pipeline inference result before ISP and after ISP in different datasets.

The restored, ISP-processed image for monitor data is shown in Fig. S10, we find that not only the color and contrast but also detail are very close to the ground truth image. This proves that our pipeline can matches very well with the smartphone ISP. The color and contrast are very natural and very similar to the ground truth. We can just replace the degraded image with the restored image, and without change or adjust too many other modules in the whole smartphone ISP.

As shown in Table 2, after processing by the ISP, the restored image even has a higher PSNR value than the raw restored image. We think it is because some of the image enhancement operations in the ISP, like the denoiser, perform further improvements of the restored image. The CIEDE2000 is a metric that can used to measure the color difference. We need to note that after ISP processing, the CIEDE2000 metric is worse than for the raw reconstruction. This illustrates further how sensitive the ISP can be to even minute changes in the raw image.

	Monitor Pretrained Model				Fine-tuning Model			
	PSNR	SSIM	LPIPS	CIEDE2000	PSNR	SSIM	LPIPS	CIEDE2000
Degraded Image	28.42	0.86	0.140	0.056	28.42	0.86	0.140	0.056
PDCRN	26.70	0.71	0.224	4.261	29.21	0.88	0.224	2.551
Our	29.34	0.76	0.101	0.052	31.40	0.91	0.128	0.039

Table 3. Fine-tune before and after result

6.2. Real World Data Result

Moving on to real-world data, we first tested the monitor dataset pretrained model on the real-world images without fine-tuning. The result is shown in supplement Fig. S12 second column. As can be seen, the small characters in the poster of the second column are a little blurry – even a little more blurry than the input image. All the papers based on ECCV 2020 UDC challenge [27, 29, 11, 38] are all only trained in the monitor-captured dataset, which we think may have similar problems. The reason may cause this and more detail about this is explained in the supplement. To solve the above imperfections of the monitor data, and further improve the result in the real practical application, we fine-tune the training with real-world data.

The fine-tuning result can be seen in the Supplement, Fig. S12. The blur problem in the small characters is resolved, which proves that our network after fine-tuning can address the deblurring task.

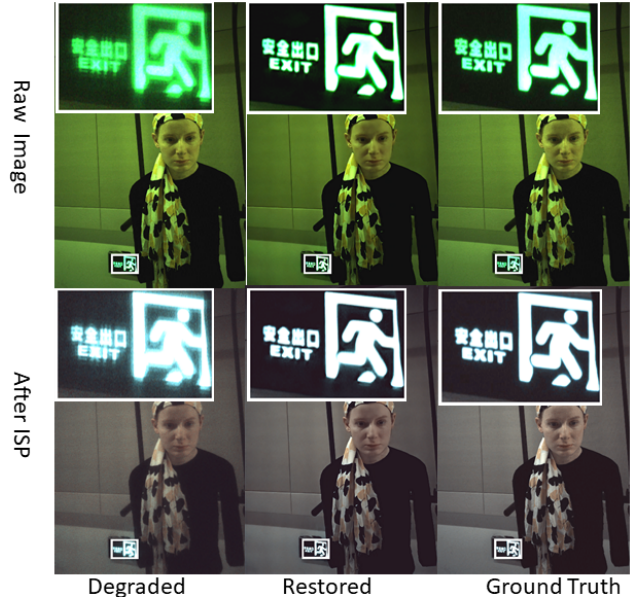


Figure 4. Real world raw data and ISP-processed result. The green image is the raw image. It is demosaicked raw data image. The ISP-proceed image is the image that go through ISP. Our restored image match with the Huawei ISP.

After passing through our restoration pipeline and the smartphone ISP, the final result is shown in the Fig. 4. As shown in the figure, some diffraction artifacts can be observed from Fig. 4 “EXIT” logo in the degraded image of the second example. There are some stripes in the bright



Figure 5. Quantitative comparison with state-of-art methods. We can see from the figure that our method restores more detail in the small characters. The PSNR and SSIM is computed in the ISP-proceed image.

green words. They are removed in the restored image. The detail of the restored image is almost the same as ground truth. In addition, because the noise model is related to the sensor, most of the time the denoising module would be deployed in the raw domain. Therefore, in our raw domain algorithm, we also consider the noise problem, and did the denoising work as well. We note that the PSNR and SSIM results for the real world data are not quite as good as for the monitor data, although the visual quality is very good. We believe this may in part be due to residual misalignment in the real world image pairs giving artificially lower ratings.

We did a comparison for some state-of-art methods similar to our task. The IDiffNet [17] and AttentionUNet [21] are some state-of-art dehazing or descattering neural residual network. Note that we use VGG loss plus SSIM loss in IDiffNet and AttentionUNet. All have been pretrained and fine-tunes using our dataset. We can see from Fig. 5, that our method restored more detail of the small character. Table 4 is the comparison result with preview dehazing or descattering neural network. We can find that our method has the best PSNR and SSIM result. Note that all metrics in Table 4 are computed based on the raw image.

7. Conclusion

In this paper, we solve a real-world image-reconstruction problem and support high image quality from under-display cameras, a new emerging camera technology for consumer devices. We propose a new raw-to-raw pipeline that allows

	PSNR \uparrow	SSIM \uparrow	LPIPS \downarrow
Degraded Image	27.6735	0.8506	0.2024
IDiffNet	28.9234	0.8722	0.1737
AttentionUNet	29.1389	0.9018	0.1420
PDCRN	29.2126	0.8813	0.2241
Ours	31.2155	0.9023	0.0994

Table 4. State-of-Art Dehazing Method Comparison. The parameter is the parameter of whole model. All metrics are computed by 3072×2048 size image.

us to make use of the off-the-shelf smartphone ISP without modifications. Instead of directly training on ISP-processed image datasets, our raw-to-raw pipeline can avoid situations where the degraded image and ground truth image go to different branches of the ISP which would tremendously complicate the training of the reconstruction network.

In addition to this core contribution, we also develop innovative solutions for data collection using an HDR display, and for synthesizing HDR portrait training data.

Our pipeline directly replaces the degraded raw image with the restored raw image without changing other modules. Our pipeline has very good performance on the raw data image, an crucially it still has good performance after applying the ISP to the restored image. The result has a very natural color, contrast, and detailed information. This proves that our pipeline can cooperate with the current off-the-shelf ISP. We believe that this raw-to-raw paradigm can be useful for many other image restoration tasks on consumer devices in the future.

References

- [1] Abdelrahman Abdelhamed, Stephen Lin, and Michael S Brown. A high-quality denoising dataset for smartphone cameras. In *Proceedings of the IEEE Conference on Computer Vision and Pattern Recognition*, pages 1692–1700, 2018.
- [2] Bolun Cai, Xiangmin Xu, Kui Jia, Chunmei Qing, and Dacheng Tao. Dehazenet: An end-to-end system for single image haze removal. *IEEE Transactions on Image Processing*, 25(11):5187–5198, 2016.
- [3] Yue Cao, Xiaohe Wu, Shuran Qi, Xiao Liu, Zhongqin Wu, and Wangmeng Zuo. Pseudo-isp: Learning pseudo in-camera signal processing pipeline from a color image denoiser. *arXiv preprint arXiv:2103.10234*, 2021.
- [4] Dongdong Chen, Mingming He, Qingnan Fan, Jing Liao, Liheng Zhang, Dongdong Hou, Lu Yuan, and Gang Hua. Gated context aggregation network for image dehazing and deraining. In *2019 IEEE Winter Conference on Applications of Computer Vision (WACV)*, pages 1375–1383. IEEE, 2019.
- [5] Yu Chen, Ying Tai, Xiaoming Liu, Chunhua Shen, and Jian Yang. Fsrnet: End-to-end learning face super-resolution with facial priors. In *Proceedings of the IEEE Conference on Computer Vision and Pattern Recognition*, pages 2492–2501, 2018.
- [6] Shechao Feng, Charles Kane, Patrick A Lee, and A Douglas Stone. Correlations and fluctuations of coherent wave transmission through disordered media. *Physical review letters*, 61(7):834, 1988.
- [7] Ishaan Gulrajani, Faruk Ahmed, Martin Arjovsky, Vincent Dumoulin, and Aaron C Courville. Improved training of wasserstein gans. In *Advances in neural information processing systems*, pages 5767–5777, 2017.
- [8] Tiantong Guo, Venkateswararao Cherukuri, and Vishal Monga. Dense123’ color enhancement dehazing network. In *Proceedings of the IEEE Conference on Computer Vision and Pattern Recognition Workshops*, pages 0–0, 2019.
- [9] Kaiming He, Jian Sun, and Xiaoou Tang. Single image haze removal using dark channel prior. *IEEE transactions on pattern analysis and machine intelligence*, 33(12):2341–2353, 2010.
- [10] Forrest N Iandola, Song Han, Matthew W Moskewicz, Khalid Ashraf, William J Dally, and Kurt Keutzer. Squeezenet: Alexnet-level accuracy with 50x fewer parameters and 0.5 mb model size. *arXiv preprint arXiv:1602.07360*, 2016.
- [11] Andrey Ignatov, Cheng-Ming Chiang, Hsien-Kai Kuo, Anastasia Sycheva, and Radu Timofte. Learned smartphone isp on mobile npus with deep learning, mobile ai 2021 challenge: Report. In *Proceedings of the IEEE/CVF Conference on Computer Vision and Pattern Recognition*, pages 2503–2514, 2021.
- [12] Andrey Ignatov, Luc Van Gool, and Radu Timofte. Replacing mobile camera isp with a single deep learning model. In *Proceedings of the IEEE/CVF Conference on Computer Vision and Pattern Recognition Workshops*, pages 536–537, 2020.
- [13] Phillip Isola, Jun-Yan Zhu, Tinghui Zhou, and Alexei A Efros. Image-to-image translation with conditional adversarial networks. In *Proceedings of the IEEE conference on computer vision and pattern recognition*, pages 1125–1134, 2017.
- [14] Ori Katz, Pierre Heidmann, Mathias Fink, and Sylvain Gigan. Non-invasive single-shot imaging through scattering layers and around corners via speckle correlations. *Nature photonics*, 8(10):784–790, 2014.
- [15] Orest Kupyn, Volodymyr Budzan, Mykola Mykhailych, Dmytro Mishkin, and Jiří Matas. Deblurgan: Blind motion deblurring using conditional adversarial networks. In *Proceedings of the IEEE conference on computer vision and pattern recognition*, pages 8183–8192, 2018.
- [16] Boyi Li, Xiulian Peng, Zhangyang Wang, Jizheng Xu, and Dan Feng. Aod-net: All-in-one dehazing network. In *Proceedings of the IEEE international conference on computer vision*, pages 4770–4778, 2017.
- [17] Shuai Li, Mo Deng, Justin Lee, Ayan Sinha, and George Barbastathis. Imaging through glass diffusers using densely connected convolutional networks. *Optica*, 5(7):803–813, 2018.
- [18] M Ronnier Luo, Guihua Cui, and Bryan Rigg. The development of the cie 2000 colour-difference formula: Ciede2000. *Color Research & Application: Endorsed by Inter-Society Color Council, The Colour Group (Great Britain), Canadian Society for Color, Color Science Association of Japan, Dutch Society for the Study of Color, The Swedish Colour Centre Foundation, Colour Society of Australia, Centre Français de la Couleur*, 26(5):340–350, 2001.
- [19] Ezio Malis and Manuel Vargas. *Deeper understanding of the homography decomposition for vision-based control*. PhD thesis, INRIA, 2007.
- [20] Seungjun Nah, Tae Hyun Kim, and Kyoung Mu Lee. Deep multi-scale convolutional neural network for dynamic scene deblurring. In *Proceedings of the IEEE Conference on Computer Vision and Pattern Recognition*, pages 3883–3891, 2017.
- [21] Ozan Oktay, Jo Schlemper, Loic Le Folgoc, Matthew Lee, Mattias Heinrich, Kazunari Misawa, Kensaku Mori, Steven McDonagh, Nils Y Hammerla, Bernhard Kainz, et al. Attention u-net: Learning where to look for the pancreas. *arXiv preprint arXiv:1804.03999*, 2018.
- [22] Sang-Hee Ko Park, Minki Ryu, Chi-Sun Hwang, Shinhyuk Yang, Chunwon Byun, Jeong-Ik Lee, Jaeheon Shin, Sung Min Yoon, Hye Yong Chu, Kyoung Ik Cho, et al. 42.3: Transparent zno thin film transistor for the application of high aperture ratio bottom emission am-oled display. In *SID Symposium Digest of Technical Papers*, volume 39, pages 629–632. Wiley Online Library, 2008.
- [23] Yifan Peng, Qilin Sun, Xiong Dun, Gordon Wetzstein, Wolfgang Heidrich, and Felix Heide. Learned large field-of-view imaging with thin-plate optics. *ACM Trans. Graph.*, 38(6):219–1, 2019.
- [24] SM Popoff, G Leroose, R Carminati, M Fink, AC Boccara, and S Gigan. Measuring the transmission matrix in optics: an approach to the study and control of light propagation in disordered media. *Physical review letters*, 104(10):100601, 2010.

- [25] Mushfiquir Rouf, Rafal Mantiuk, Wolfgang Heidrich, Matthew Trentacoste, and Cheryl Lau. Glare encoding of high dynamic range images. In *CVPR 2011*, pages 289–296. IEEE, 2011.
- [26] Helge Seetzen, Wolfgang Heidrich, Wolfgang Stuerzlinger, Greg Ward, Lorne Whitehead, Matthew Trentacoste, Abhijeet Ghosh, and Andrejs Vorozcovs. High dynamic range display systems. pages 760–768, 2004.
- [27] Hrishikesh Panikkasseril Sethumadhavan, Densen Puthussery, Melvin Kuriakose, and Jiji Charangatt Victor. Transform domain pyramidal dilated convolution networks for restoration of under display camera images. In *European Conference on Computer Vision*, pages 364–378. Springer, 2020.
- [28] Qilin Sun, Ethan Tseng, Qiang Fu, Wolfgang Heidrich, and Felix Heide. Learning rank-1 diffractive optics for single-shot high dynamic range imaging. In *Proceedings of the IEEE/CVF Conference on Computer Vision and Pattern Recognition*, pages 1386–1396, 2020.
- [29] Varun Sundar, Sumanth Hegde, Divya Kothandaraman, and Kaushik Mitra. Deep atrous guided filter for image restoration in under display cameras. In *European Conference on Computer Vision*, pages 379–397. Springer, 2020.
- [30] Antoine Toisoul and Abhijeet Ghosh. Practical acquisition and rendering of diffraction effects in surface reflectance. *ACM Transactions on Graphics (TOG)*, 36(5):1–16, 2017.
- [31] Xiangyu Xu, Yongrui Ma, and Wenxiu Sun. Towards real scene super-resolution with raw images. In *Proceedings of the IEEE/CVF Conference on Computer Vision and Pattern Recognition*, pages 1723–1731, 2019.
- [32] Anqi Yang and Aswin Sankaranarayanan. Designing display pixel layouts for under-panel cameras. *IEEE Transactions on Pattern Analysis and Machine Intelligence*, 2021.
- [33] Qirui Yang, Yihao Liu, Jigang Tang, and Tao Ku. Residual and dense unet for under-display camera restoration. In *European Conference on Computer Vision*, pages 398–408. Springer, 2020.
- [34] Xuaner Zhang, Qifeng Chen, Ren Ng, and Vladlen Koltun. Zoom to learn, learn to zoom. In *Proceedings of the IEEE/CVF Conference on Computer Vision and Pattern Recognition*, pages 3762–3770, 2019.
- [35] Zhenhua Zhang. Image deblurring of camera under display by deep learning. In *SID Symposium Digest of Technical Papers*, volume 51, pages 43–46, 2020.
- [36] Hang Zhao, Orazio Gallo, Iuri Frosio, and Jan Kautz. Loss functions for image restoration with neural networks. *IEEE Transactions on computational imaging*, 3(1):47–57, 2016.
- [37] Yuqian Zhou, Michael Kwan, Kyle Tolentino, Neil Emerton, Sehoon Lim, Tim Large, Lijiang Fu, Zhihong Pan, Baopu Li, Qirui Yang, et al. Udc 2020 challenge on image restoration of under-display camera: Methods and results. *arXiv preprint arXiv:2008.07742*, 2020.
- [38] Yuqian Zhou, David Ren, Neil Emerton, Sehoon Lim, and Timothy Large. Image restoration for under-display camera. *arXiv preprint arXiv:2003.04857*, 2020.
- [39] Jun-Yan Zhu, Taesung Park, Phillip Isola, and Alexei A Efros. Unpaired image-to-image translation using cycle-consistent adversarial networks. In *Proceedings of the IEEE international conference on computer vision*, pages 2223–2232, 2017.

ISP-Agnostic Image Reconstruction for Under-Display Cameras Supplement



Figure S1. ISP non-linearity. The first column is brightness change caused by smartphone ISP multi-frame fusion. The dark part of background become bright after multi-frame fusion. The second column is smartphone ISP auto white balance operation. The boy face change from blue to yellow. The third column is smartphone ISP dynamic range correction, the image change from dark to bright.

S1. ISP Nonlinearities

In Fig. S1 in the paper, we show several examples of how the ISP processing can affect the final appearance of the image. The first column shows an image pair captured from an HDR monitor. The bottom image was captured with multi-frame fusion, while the top image was shown without this operation. As can be seen, the leaf and tree trunk on the top is dark. However, on the bottom one, the same objects appear brighter. The change happens specifically because of the process of multi-frame fusion. Every pair - dark and bright area of the image – is different and the brightness change cannot be predicted without a detailed model of the ISP algorithms.

The second column depicts images that were captured of boy in front of different backgrounds. The portrait of the boy was composited over different backgrounds, and again shown on an HDR monitor for capturing (see Sec. 5.3). We note that the ISP reproduces different facial colors for the two images due to auto white balancing. Color distortions also exist between UDC and regular image pairs, so this behavior is again problematic for a training dataset.

Finally, the third column is example a high dynamic range scene. In this case, the image undergoes a dynamic range correction (DRC). This will also break the brightness consistency between the degraded image and the reference image.

S2. Dataset

S2.1. Calibration

Before capturing a large number of image pairs for training, we calibrated the system as follows: (1) we displayed checkerboard patterns on the monitor and then estimated

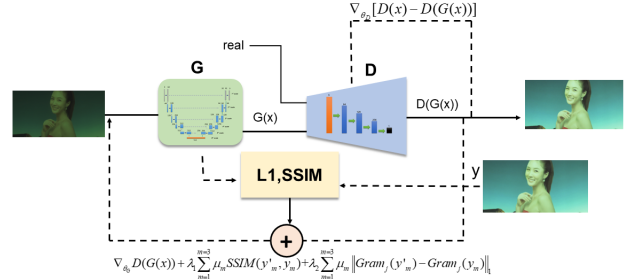


Figure S2. WGAN-GP Structure. G and D respectively stand for the generator and the discriminator. We use an optimized UNet structure for the generator, and a simple CNN for the discriminator. We add a content loss composed of SSIM and perceptual loss to constrain the generator.

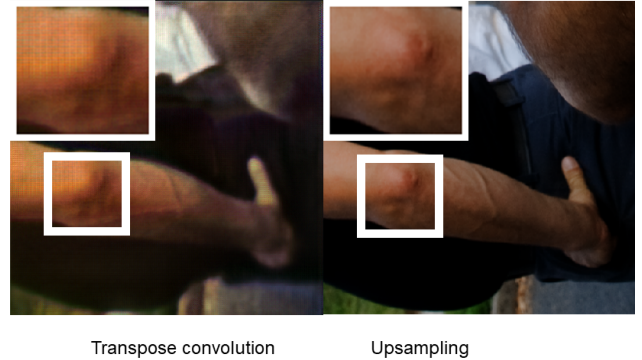


Figure S3. Transpose convolution block artifacts. The left image is restored result of transpose convolution layer. We can see clearly that there is a block artifacts in the left image. On the right is the restored result with the upsampling layer. It is much more clean and shows no block artifacts.

the camera lens's distortion parameters and the homography transform matrix between each camera and the monitor. (2) we captured the white image displayed on the monitor to compensate for the brightness non-uniformity effect of the monitor and the two cameras' vignetting effect. (3) We calibrated the display color of the HDR monitor. Since ordinary chromatic meter is unable to measure HDR signal, we adopted a complementary measurement method by using a DSLR Canon Camera 5D MarkIV and a spectral camera Specim IQ. We utilized the Canon camera to capture a stack of color sample images shown on the monitor with varying exposure time, and fused them to obtain the HDR color responses of the camera. We then used the spectral camera to measure the spectral distribution functions of the primaries of the monitor, and calculate a color transform matrix from the color responses of the Canon camera to CIE RGB values, and obtain the 3x3 color transform matrix from CIE XYZ color space to the Canon camera by capturing the three same images, and finally obtain the xyz value from the arbitrary captured color. After capturing and mon-

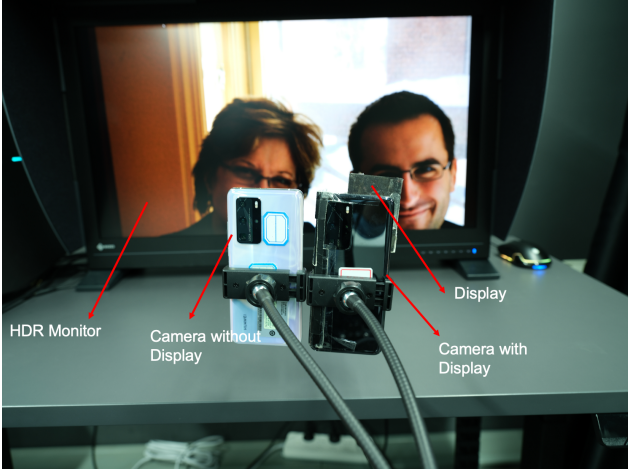


Figure S4. HDR Monitor data collection setup. Two mobile phones are placed in front of the HDR monitor, one with the UDC hardware, and one with an identical reference camera without the UDC feature. The phone is oriented vertically to mimic the most common usage case. The setup is in a dark room, and we fix the exposure time and iso setting of the cameras.

itor image, we did image registration and apply this color transform to map the captured image to correct HDR color.

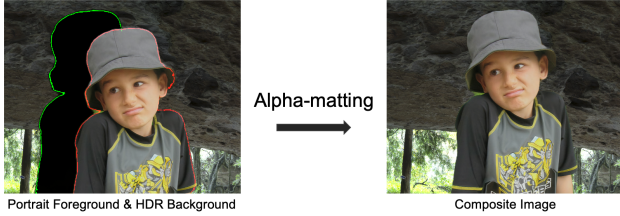


Figure S5. Portrait Image Composition.

S2.2. HDR Portrait Dataset Upsample

To fill the gaps between the resolution of the portrait images and HDR images, we utilized a portrait superresolution method [5] to enhance the resolution of portrait images and match the resolutions of the portrait and background. The result shown in the Fig. S6 The network we used for super-resolution enhance the resolution with an upsampling factor of 4. It will introduce some artifacts but these artifacts is the same for the UDC image and no UDC image, therefore, it won't cause any problem for our restoration task. The foreground and background of the chosen images are harmonious and hard to be distinguished for human eyes. The images include indoors and outdoor scenes under bright and dark light condition.

S2.3. Brightness Normalization and Compensation

Because the display absorbs some light, the shutter speed for camera with display is longer than the camera without

display. Moreover, we found it difficult to disable the auto-exposure on the mobile phone prototypes we used. Instead, we used image metadata to compensate for any differences in exposure and iso values. Specifically, we use a brightness compensation factor

$$\eta = \frac{t'}{iso} \frac{iso'}{t} \kappa, \quad (7)$$

where t is the exposure time of the image captured without display, and t' is the exposure time of the image captured with the display. iso is the ISO value of image captured without display, and iso' is the ISO value of the image captured with the display. κ is a global brightness compensation factor that approximately compensates for the brightness loss in the UDC hardware, in our case $\kappa = 0.5$. This value is determined by tuning manually and find the best result that make two images brightness match with each other.

We divided this normalization factor η for every degraded image pixel value. Then we keep a relative fixed mapping relationship between the input image and the output image, so that the neural network can learn it easily.

Note that all the smartphone raw images have a black level current. Before doing the brightness normalization and compensation we subtract the black level current first. Then do the brightness normalization and compensation based in the formula in the paper. Then go through our restoration algorithm and convert to raw image again. Finally we add the black level current back to match regular RAW images and facilitate post-processing with the smartphone ISP.

S2.4. Training and Test Detail

All the neural networks are implemented in Pytorch 1.5 and Python 3.7. All the training is done on an Nvidia Tesla V100 GPU. Due to GPU memory limitations, testing is performed on the CPU, since this allows us to load a full sized image. The generator has 2.15M parameters, and requires 160.30 GFLOPs to reconstruct a 3072×2048 image. The run time is 0.25 s for a 3072×2048 image on the Intel i7-9750H 2.6GHz CPU with 32GB memory.

S3. Result

S3.1. Ablation Study

The reason that we choose perceptual loss is because perceptual loss will preserve more texture detail and have better perceptual performance. As shown in Fig. S8, the perceptual loss restores more texture detail than the L1 loss, especially in the wall region. In addition, the L1 loss is more sensitive to misalignment in the image pairs. As shown in Table 1, the perceptual loss and SSIM loss combination is better than the L1 and SSIM loss combination.

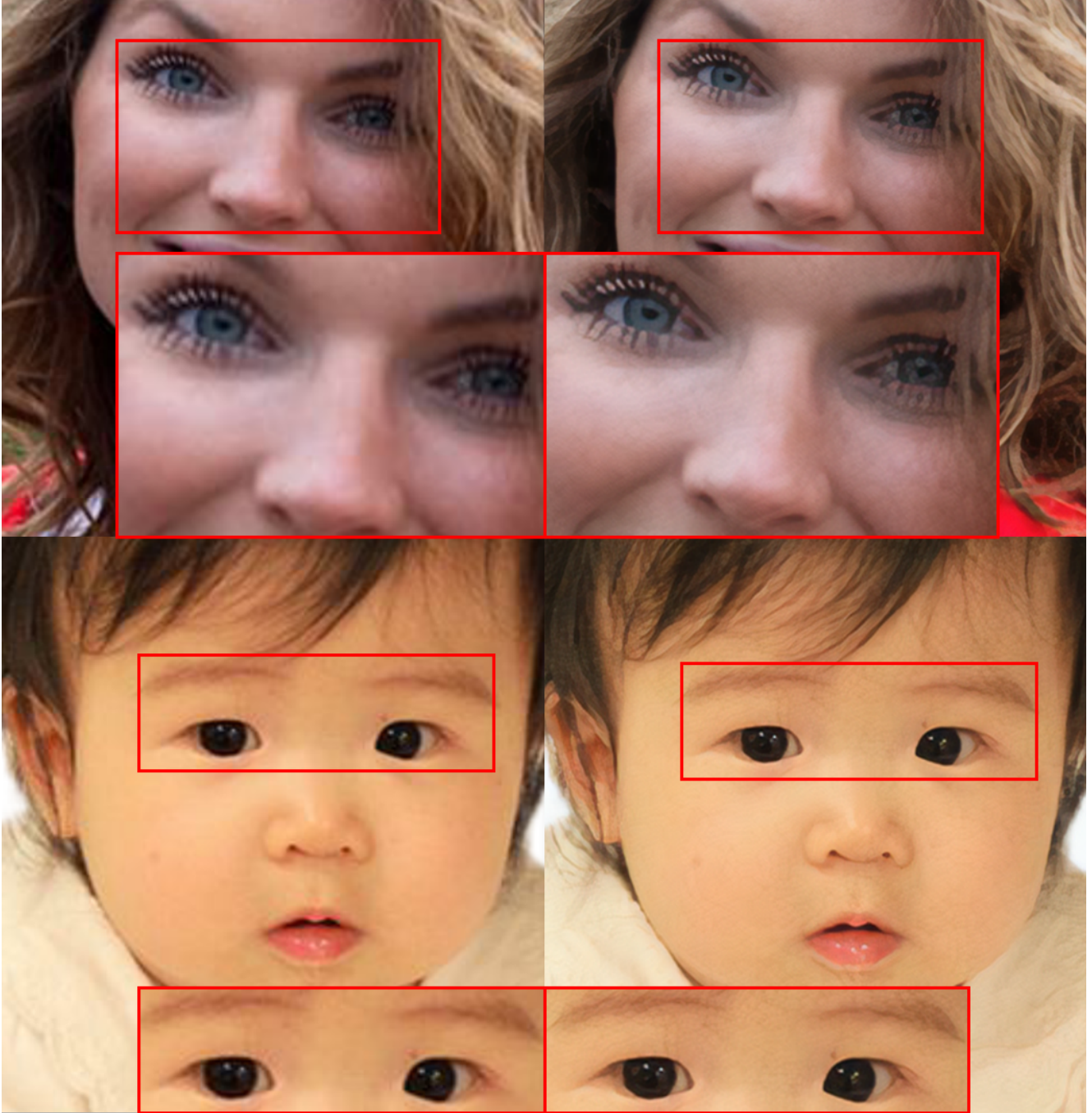


Figure S6. Upsample

S3.2. Pretrain Dataset and Fine-tune

We want to note that the zoom in patch in the Fig. S12 is very small in the full image. The monitor pretrained model performance is still overall very good. However, there is a very tiny blurry for the little detail. The Table 3 shows the result of monitor pretrained model before and after fine-tune. The PDCRN is the method [27] in the UDC chal-

lenge. We can see that both our method and PDCRN has the same problem that although monitor pretrained model can perform very well in the monitor dataset, the metrics number decrease a lot when it test in the real world dataset. There are several reasons that may account for this. First of all, the monitor image resolution is limited. It can not be as sharp and detailed as the real-world image, and therefore small texture details are lost. Second, the monitor image



Figure S7. Training the UDC restoration network on ISP-processed image pairs does not produce good results due to the black-box non-linearities in the ISP.



Figure S8. L1 Loss and perceptual loss comparison.

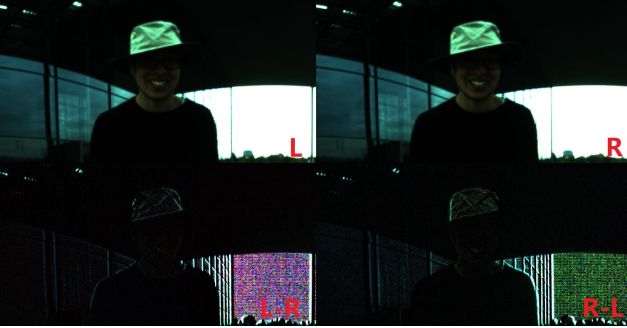


Figure S9. Monitor structured noise. This monitor image is captured by Cannon Mark IV dual pixel camera. L and R respectively refer to the left and right subimages of the dual pixel sensor, and $L - R$ refers to the amplified image difference.

suffers from some structured noise. The Fig. S9 is a captured image of HDR monitor used for creating the monitor dataset. The top row are images captured by dual pixel sensor. The bottom row are the images that difference between left view image and right view image. Consider the white sky in the background of Fig. S9. This area should be very smooth with almost constant pixel values. However the difference of two views shows there is structured noise for monitor.

S4. ISP Post-processing

For ISP processign after reconstruction, we utilize two smartphone ISPs. First is the black-box Huawei smartphone

ISP, while another is based on a simple ISP pipeline built by ourselves. In the latter The demosaicing is based on the gradient-corrected linear interpolation. The auto white balance correction algorithm is based on the paper [?]. Finally, we apply gamma correction. Our reconstructions perform equally well under both of these ISPs.

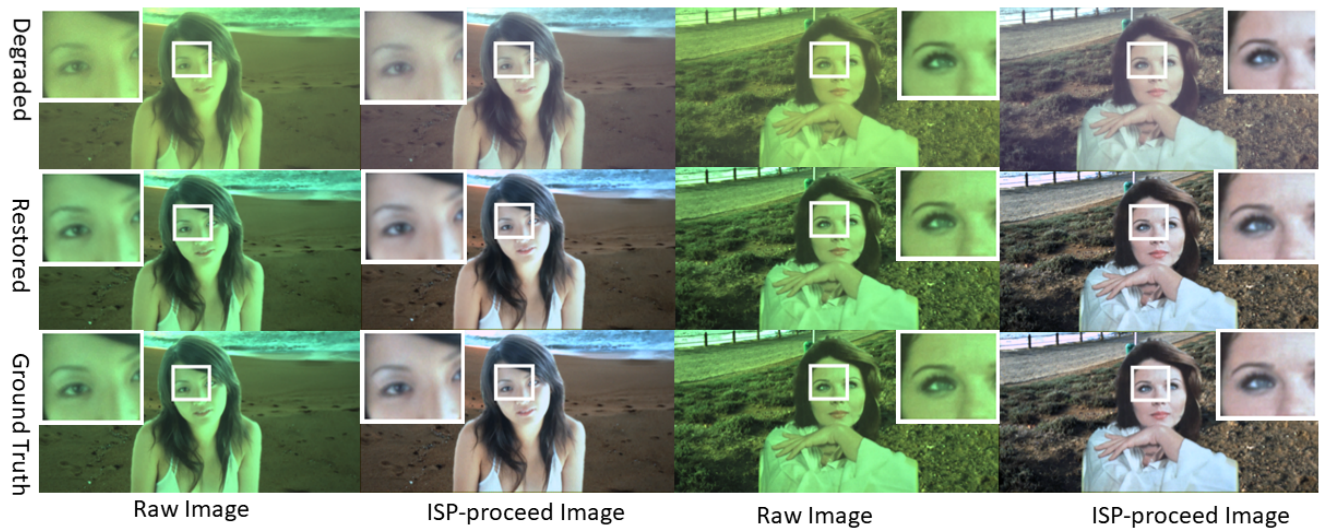


Figure S10. Monitor raw data and ISP-processed data results. The green image is the demosaicked raw image. The ISP-proceed image is the restored raw image that after passing through the ISP. Our restored UDC image matches with the ISP-processed image of the reference (non-UDC) camera.



Figure S11. Restoration result. The first column is the monitor raw dataset restoration result. The restored raw image is processed by the legacy ISP, and the output is shown in the second column. The third column is real-world test result. We can see that there is obvious stripe-like diffraction artifacts in the green words in the third column degraded image, but removed in our result.



Figure S12. Effect of fine-tuning with real-world data. From left to right: input image, restoration result for monitor pre-trained model, and restoration result using the full fine-tuned model.

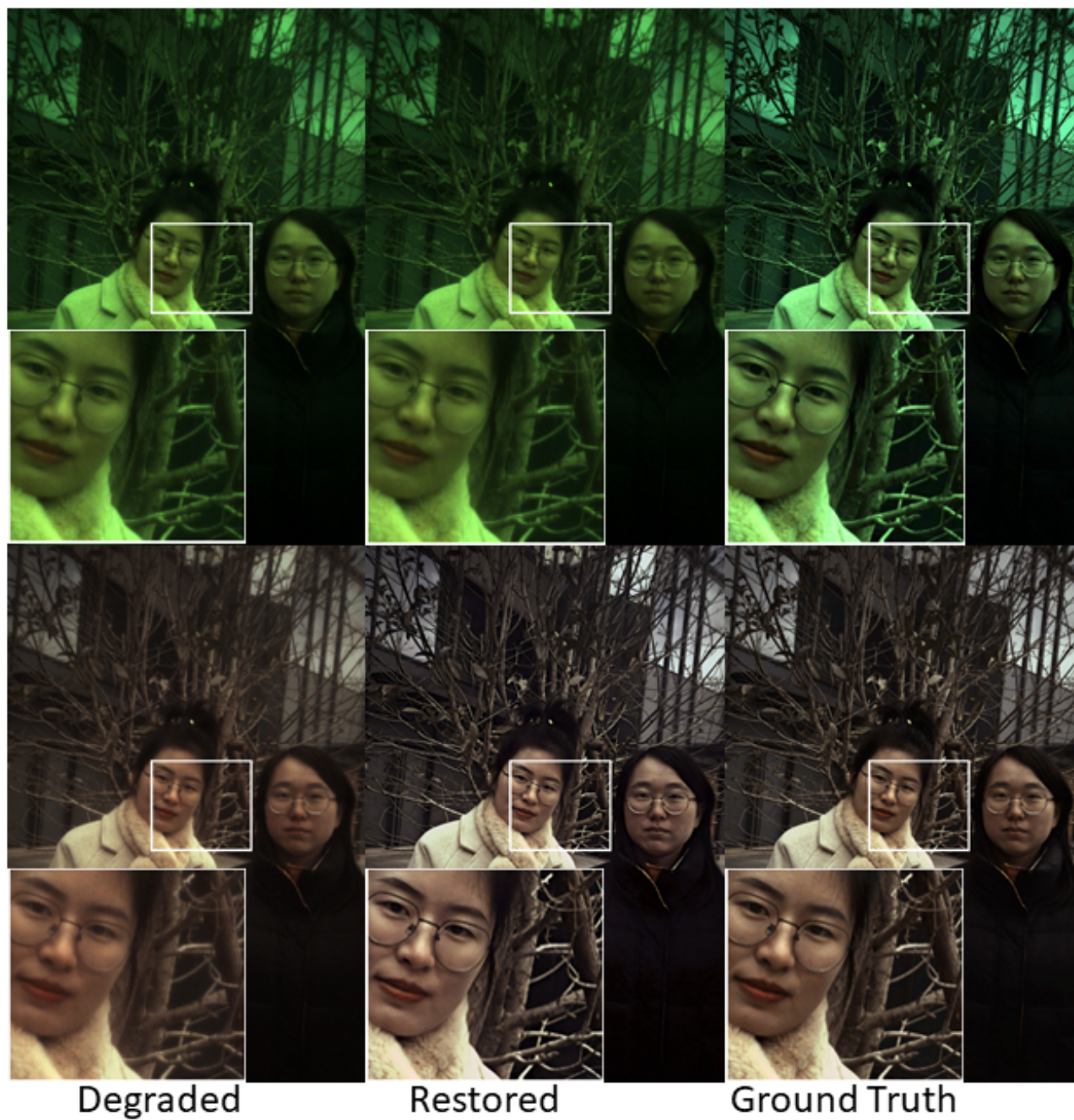


Figure S13. Some More Real World Data Results.



Figure S14. Some More Real World Data Results.



Figure S15. Some More Real World Data Results.

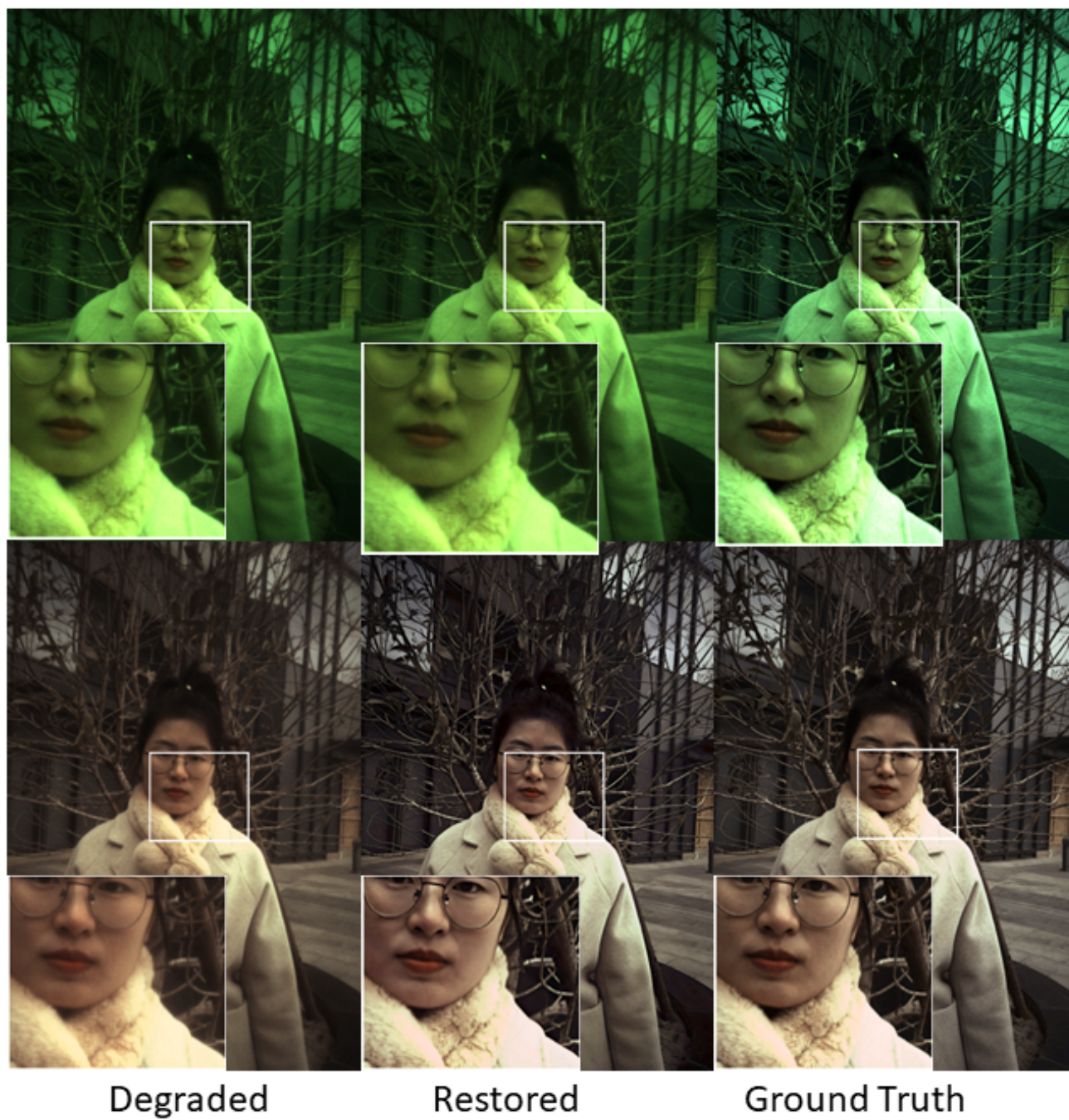
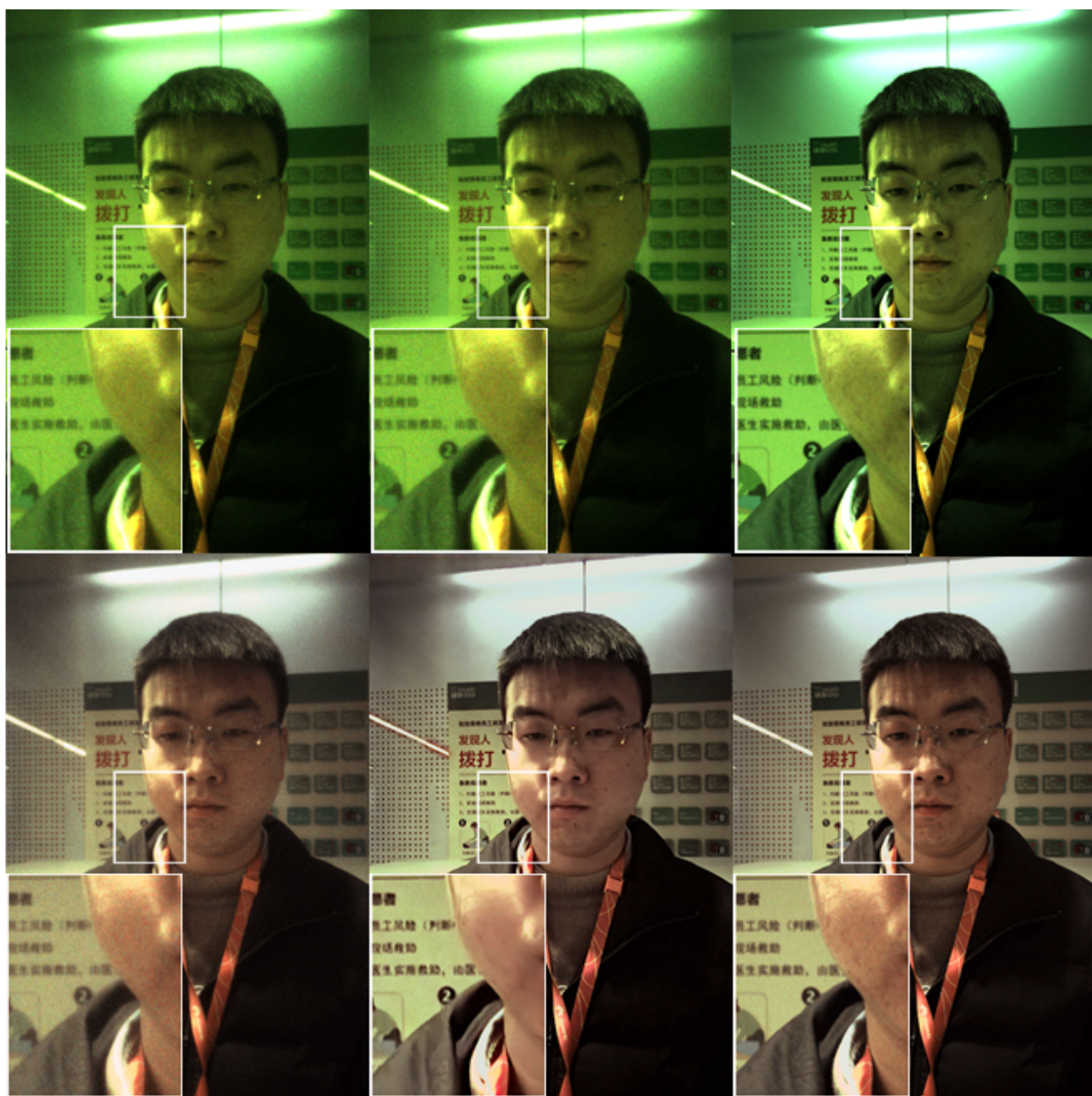


Figure S16. Some More Real World Data Results.



Degraded

Restored

Ground Truth

Figure S17. Some More Real World Data Results.

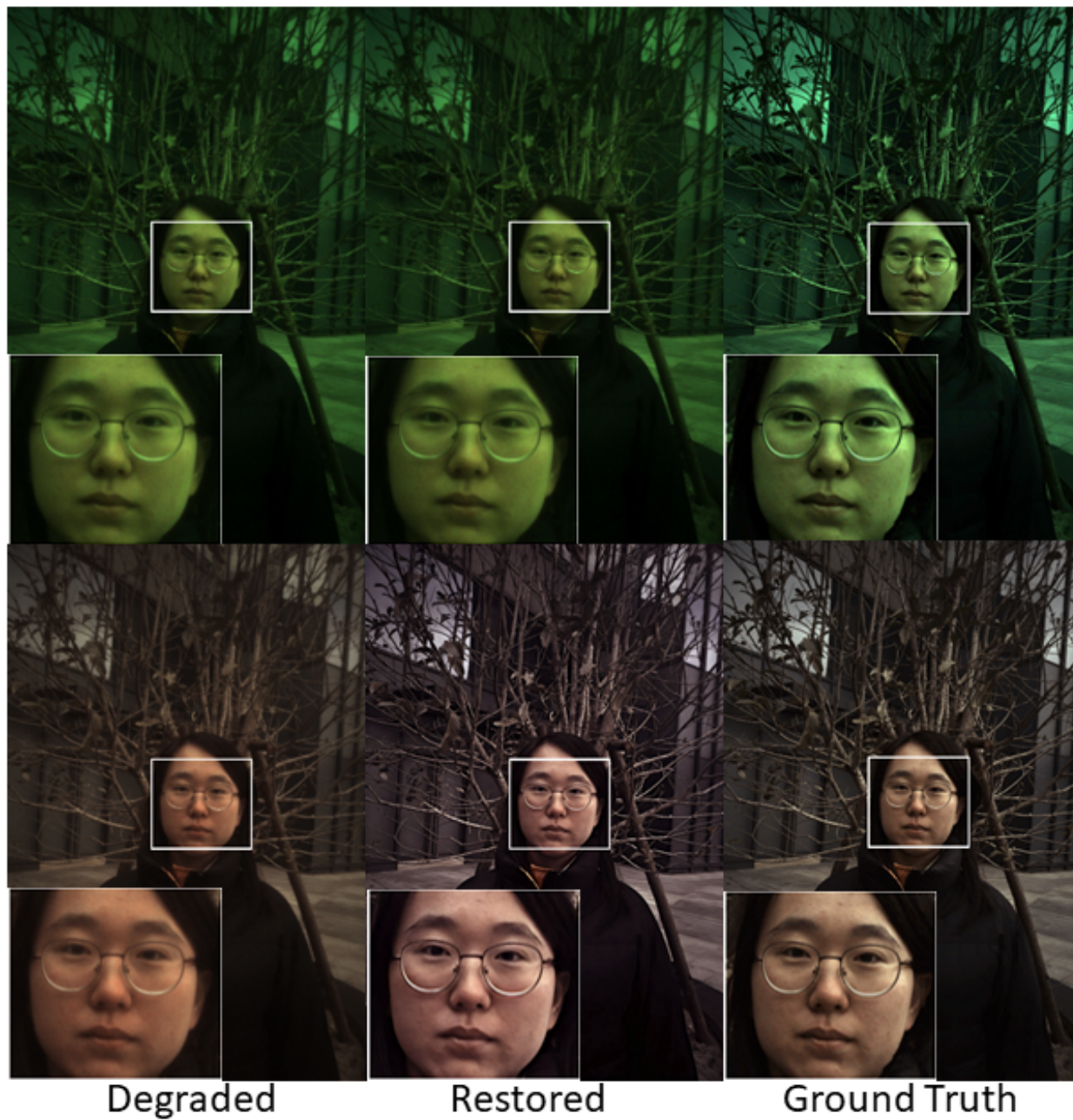


Figure S18. Some More Real World Data Results.

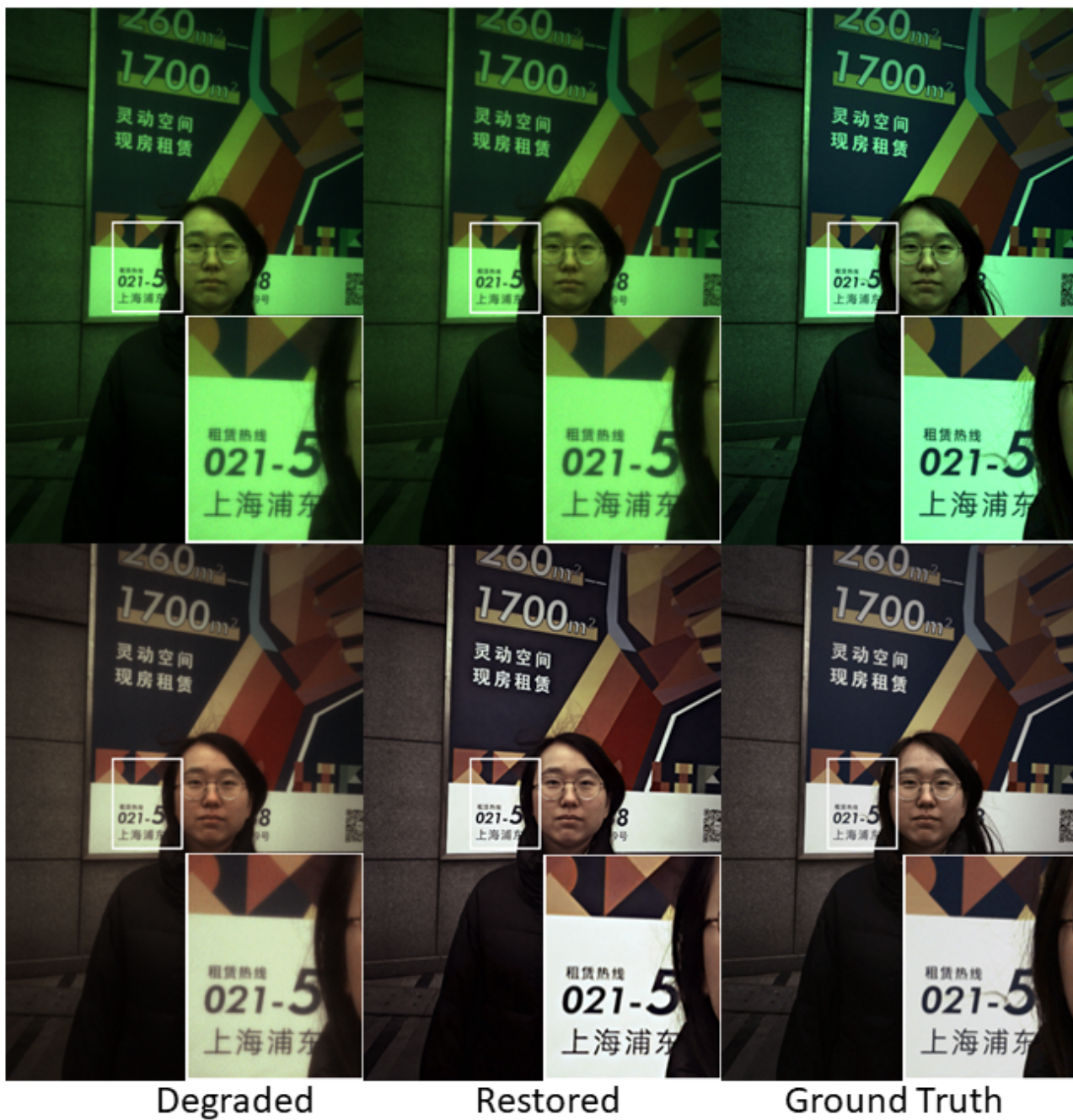


Figure S19. Some More Real World Data Results.

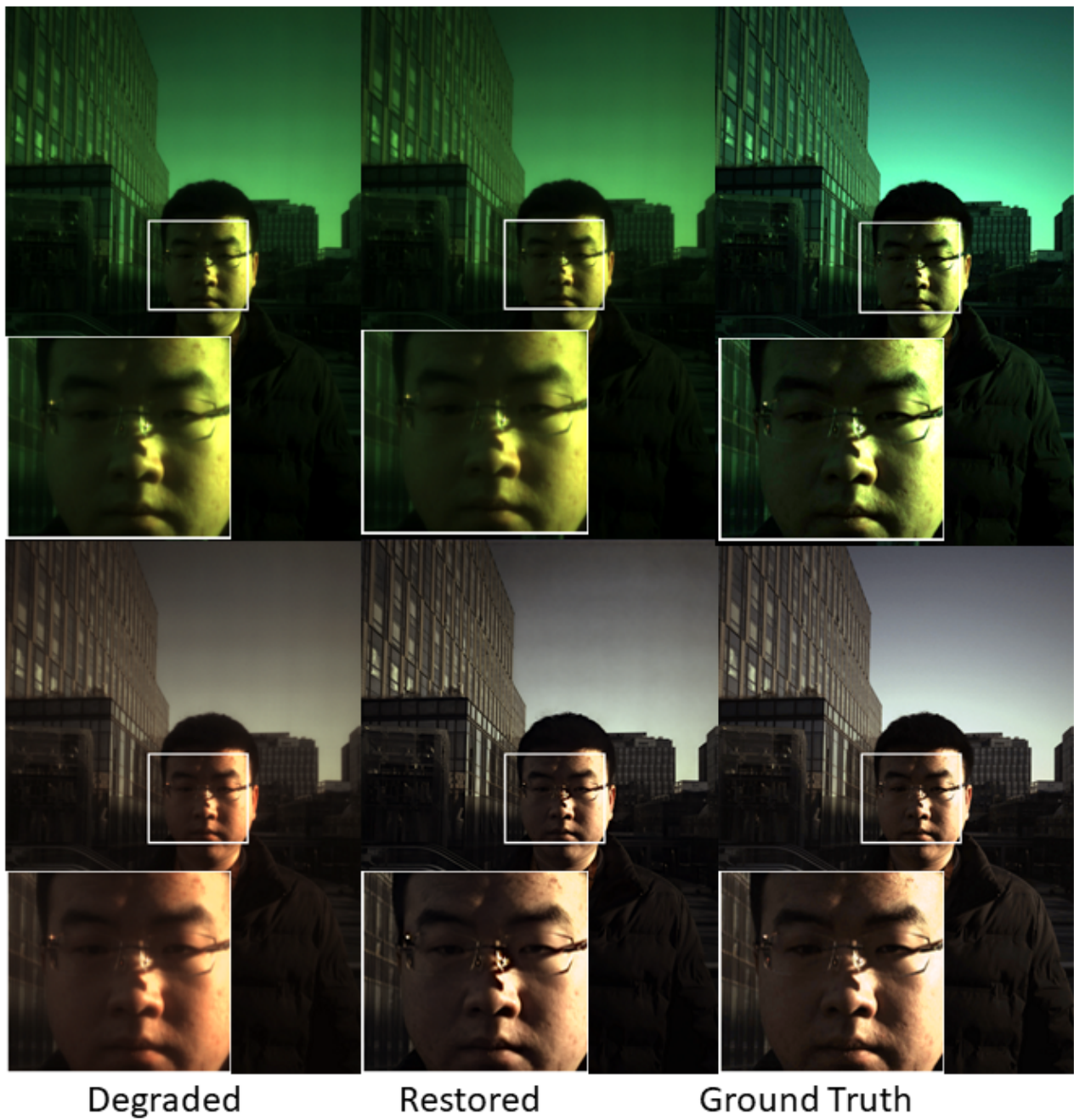
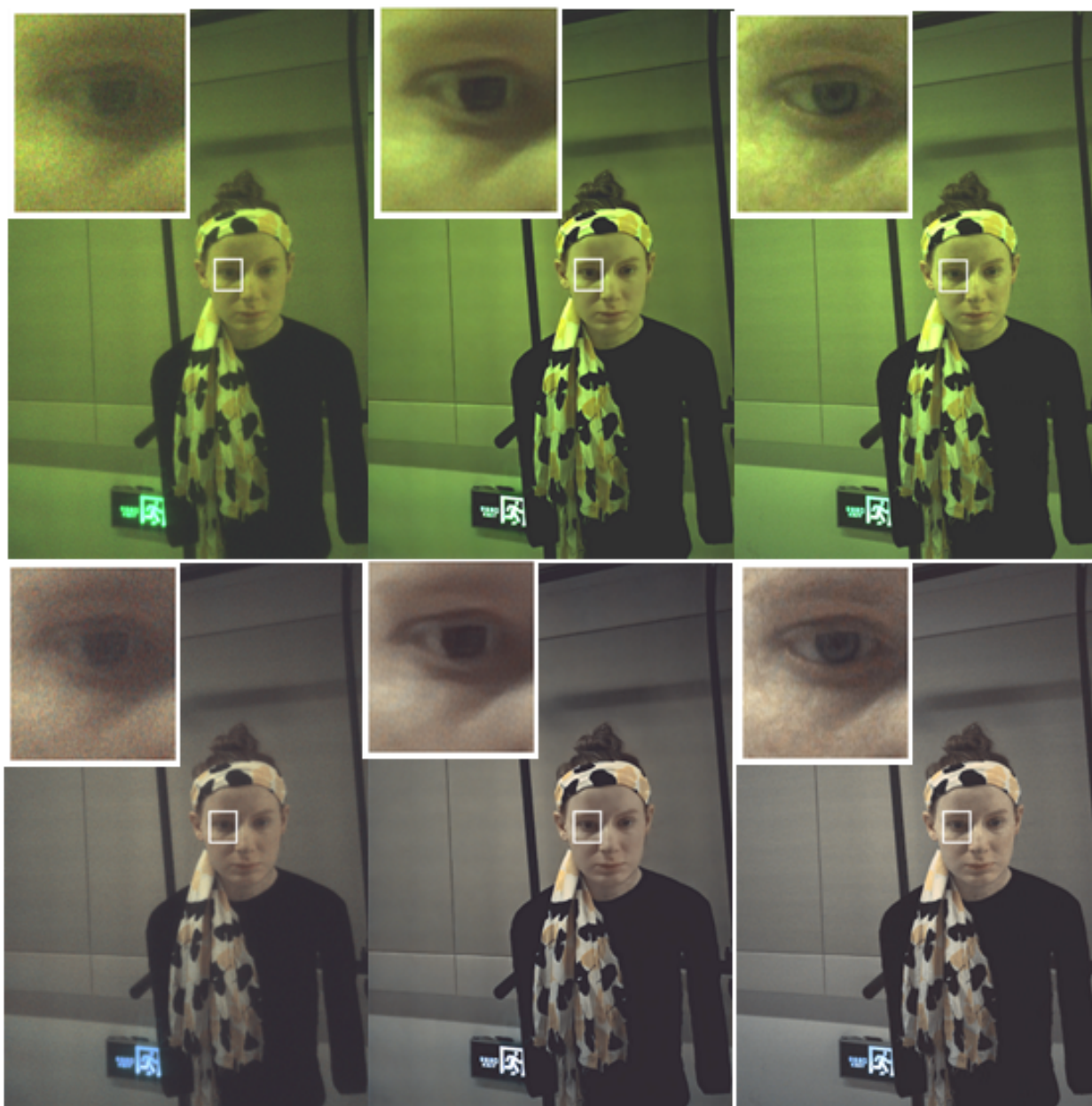


Figure S20. Some More Real World Data Results.

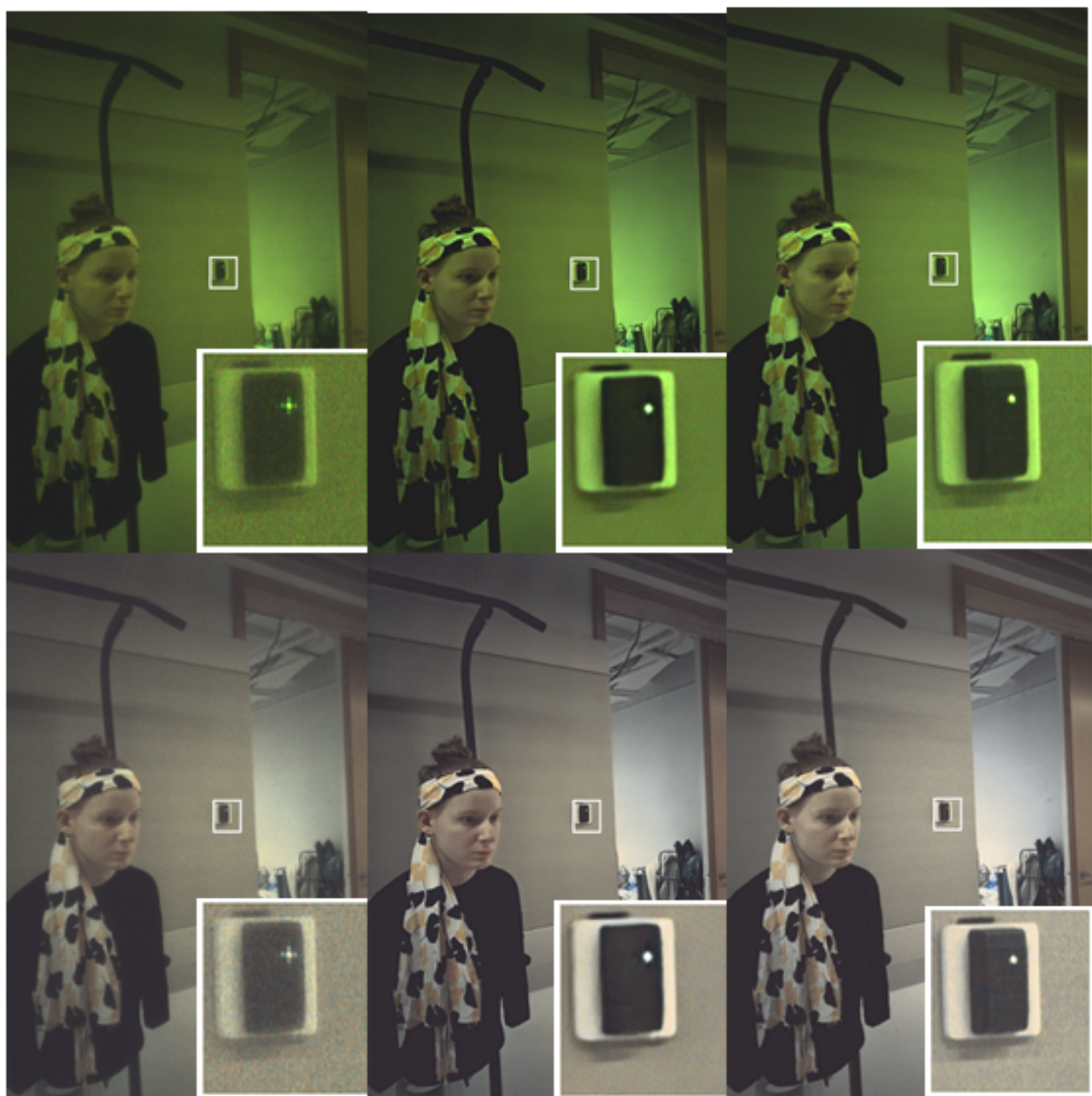


Degraded

Restored

Ground Truth

Figure S21. Some More Real World Data Results.



Degraded

Restored

Ground Truth

Figure S22. Some More Real World Data Results.

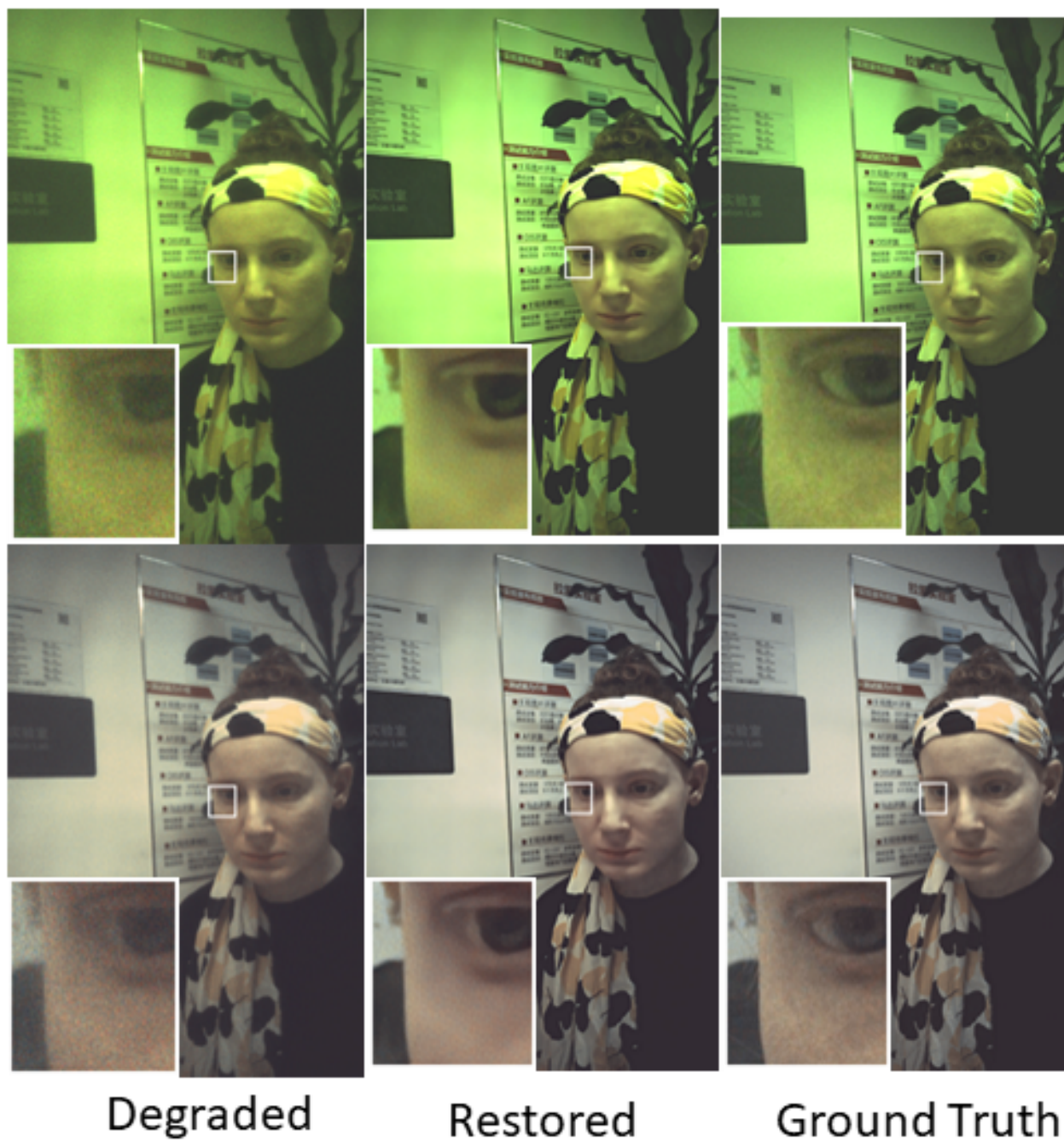


Figure S23. Some More Real World Data Results.

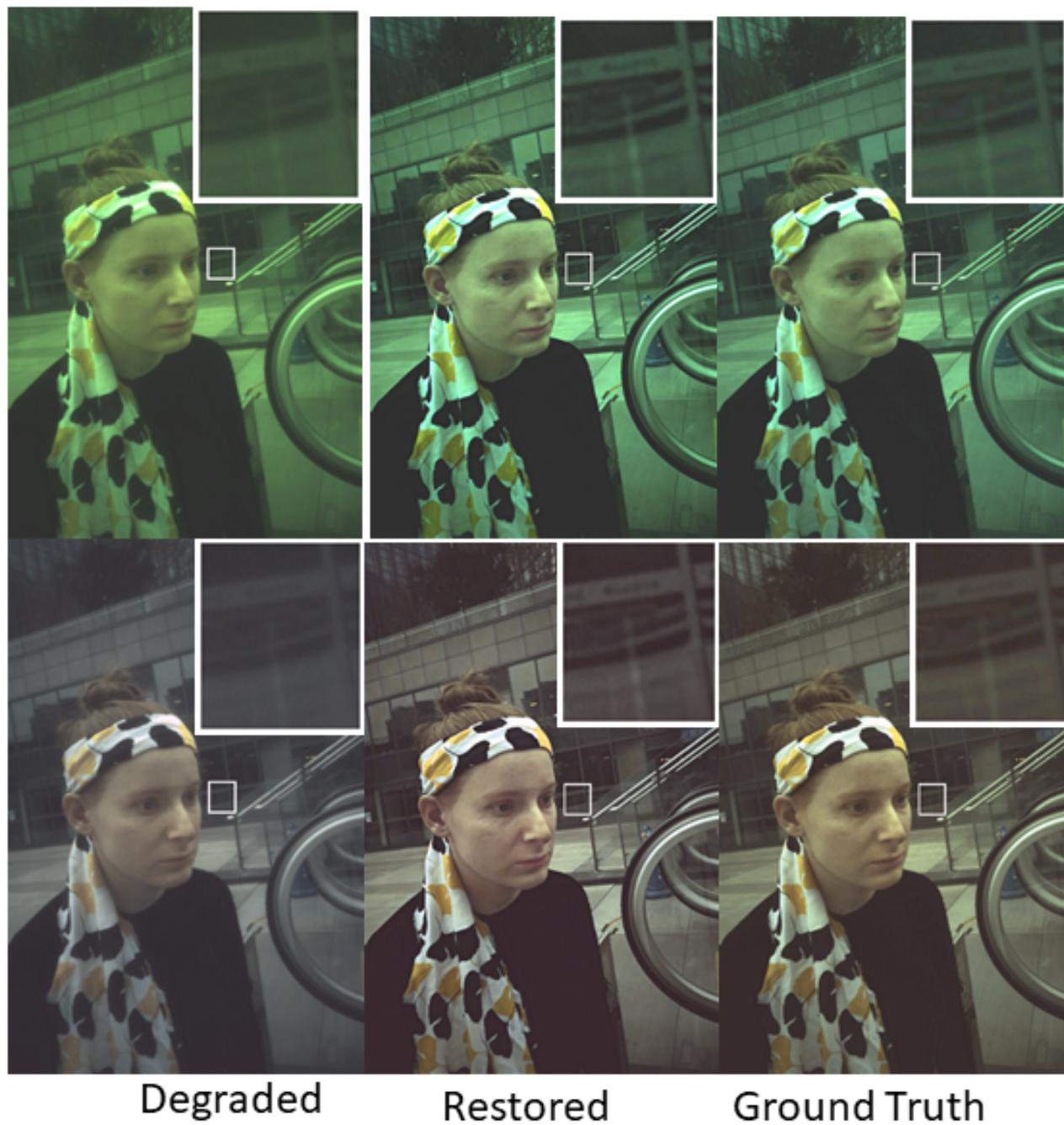


Figure S24. Some More Real World Data Results.

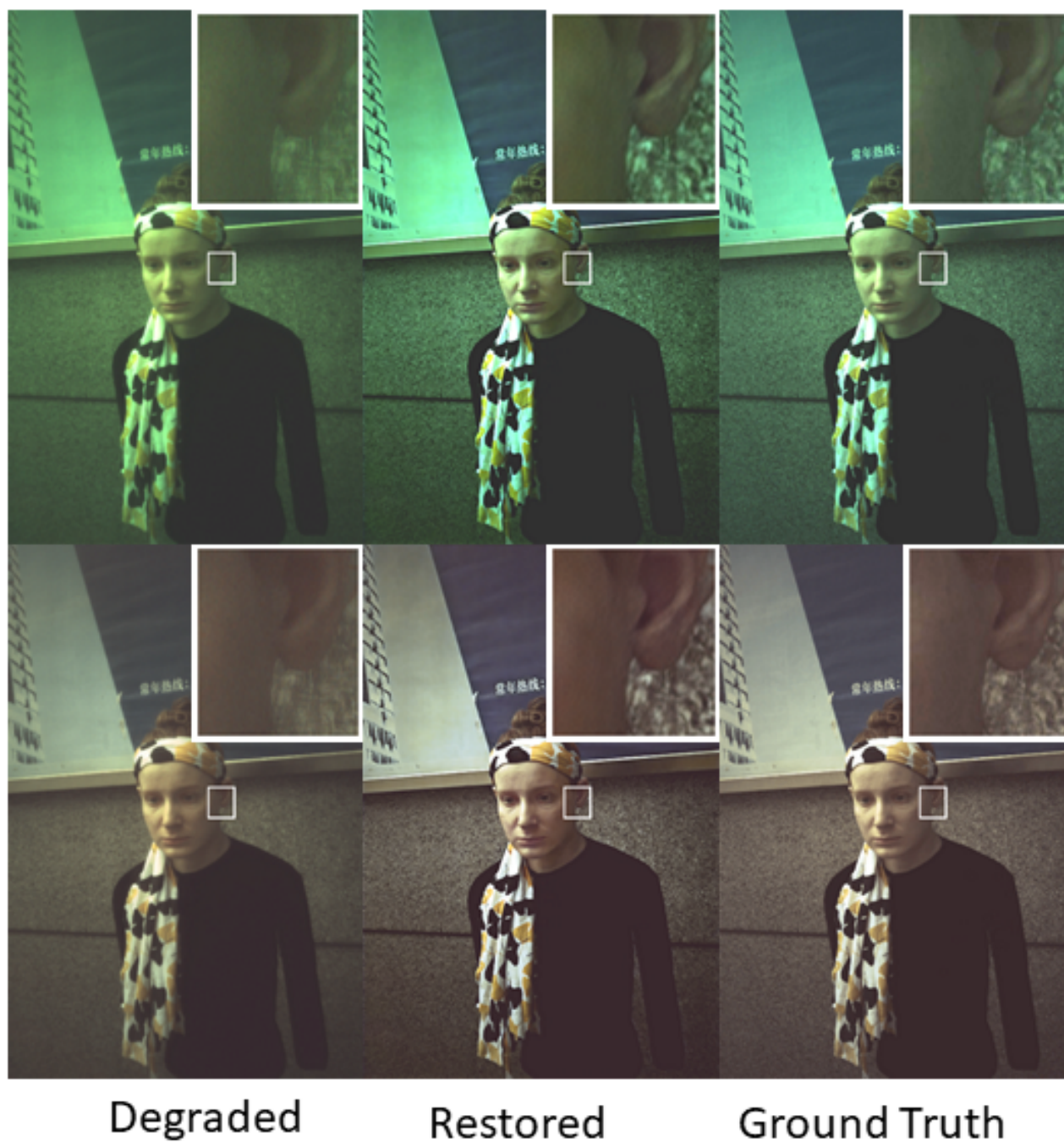


Figure S25. Some More Real World Data Results.

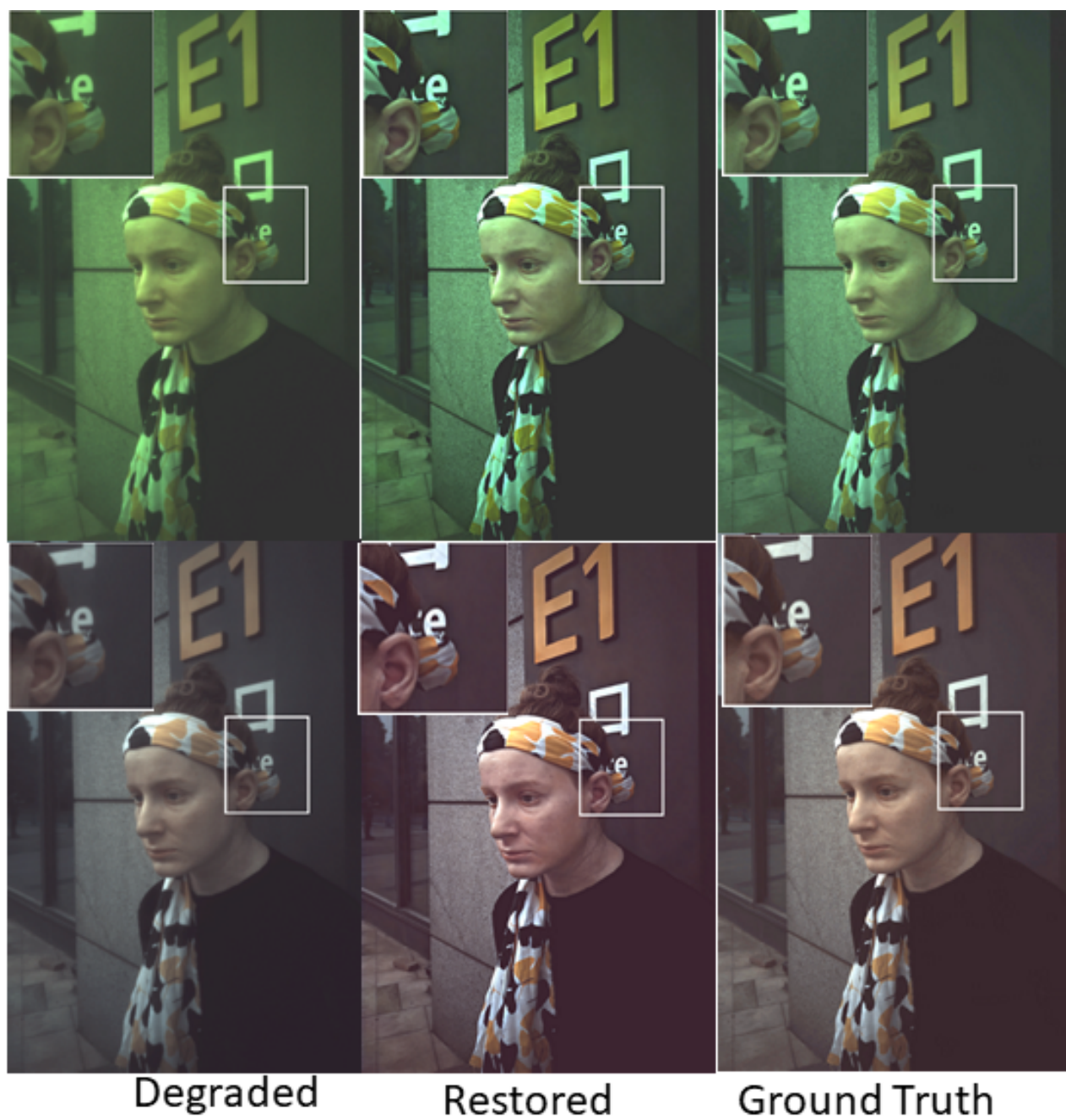


Figure S26. Some More Real World Data Results.

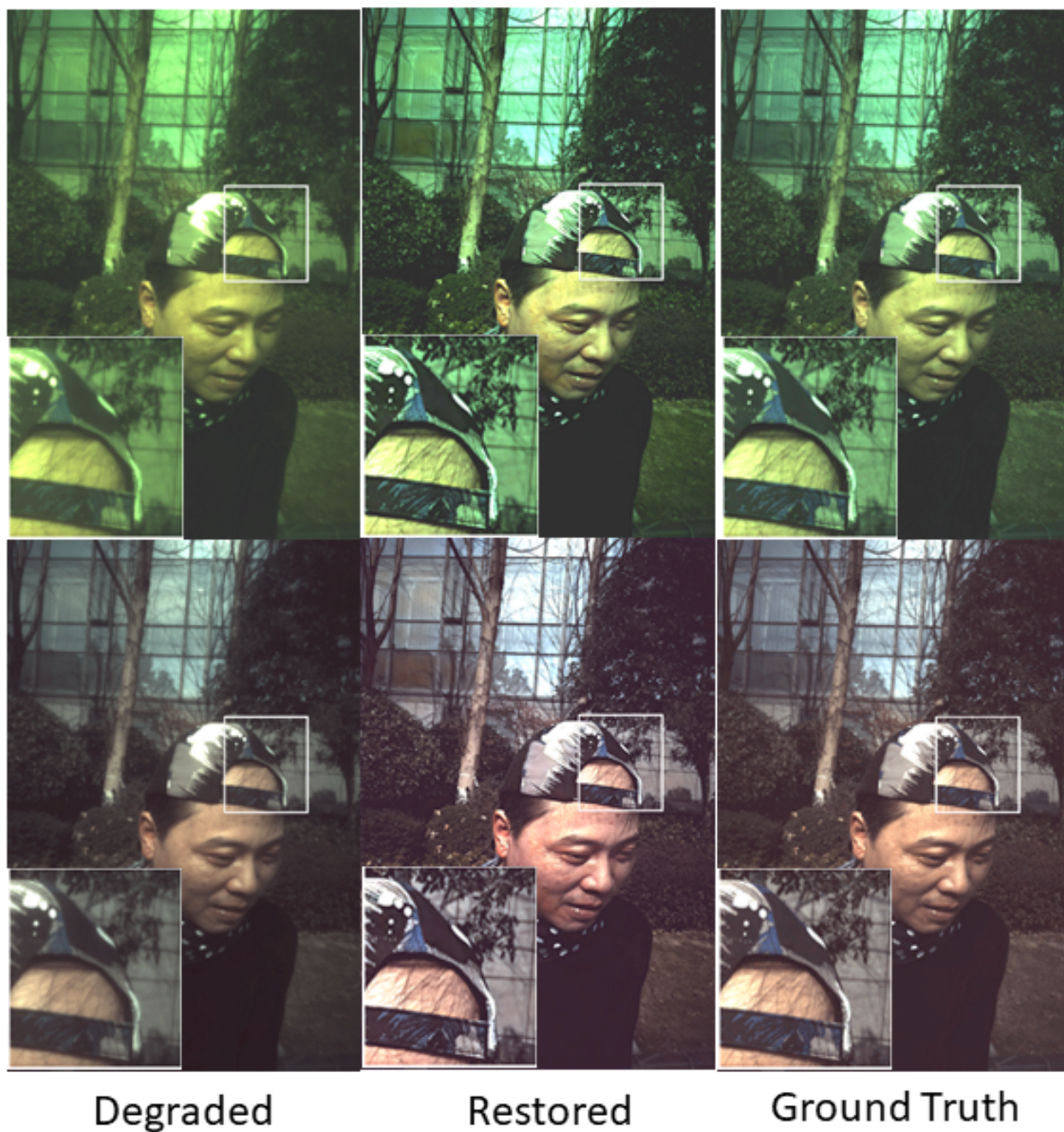


Figure S27. Some More Real World Data Results.



Figure S28. Some More Real World Data Results.

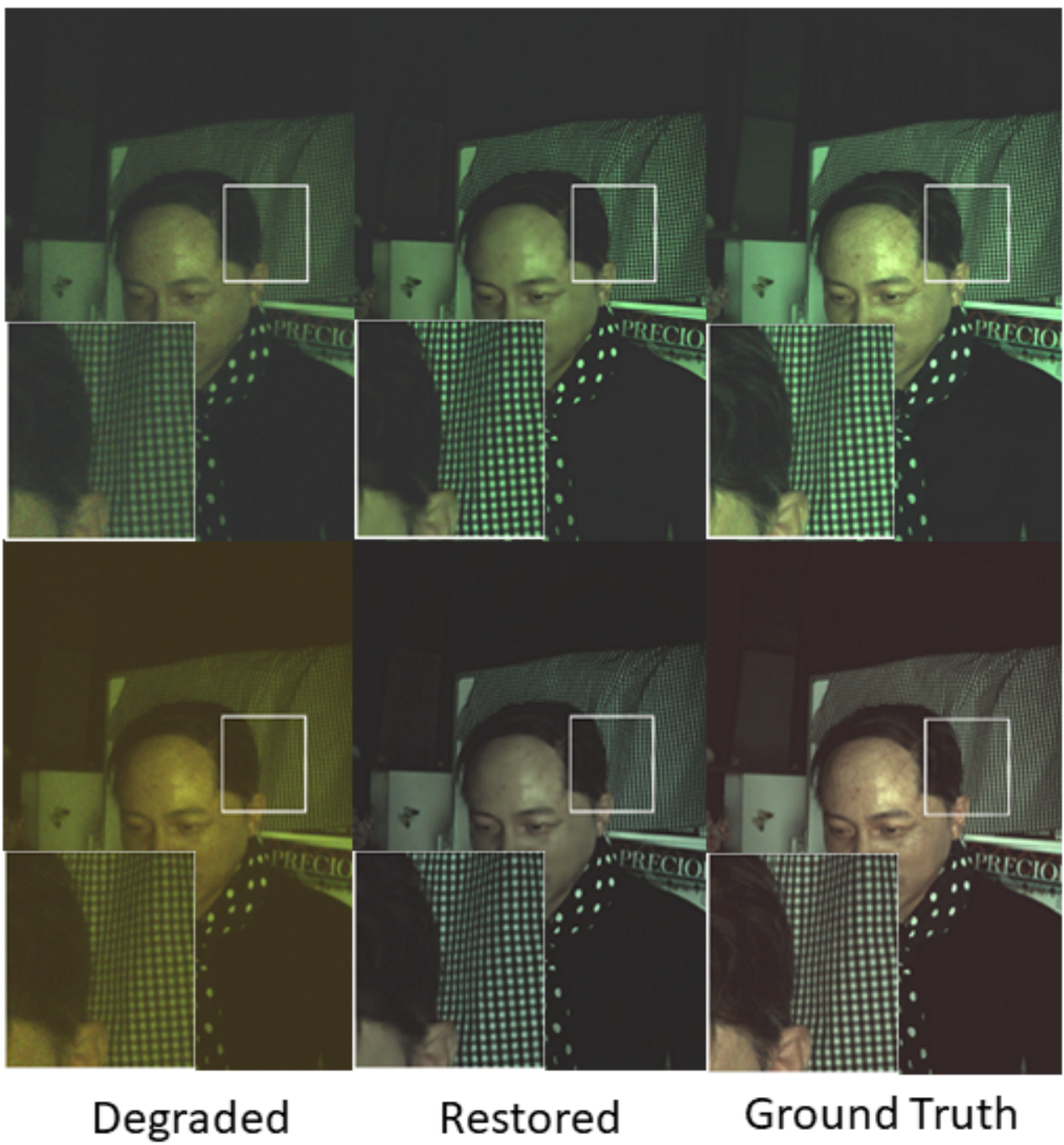


Figure S29. Some More Real World Data Results.



Degraded

Restored

Ground Truth

Figure S30. Some More Real World Data Results.

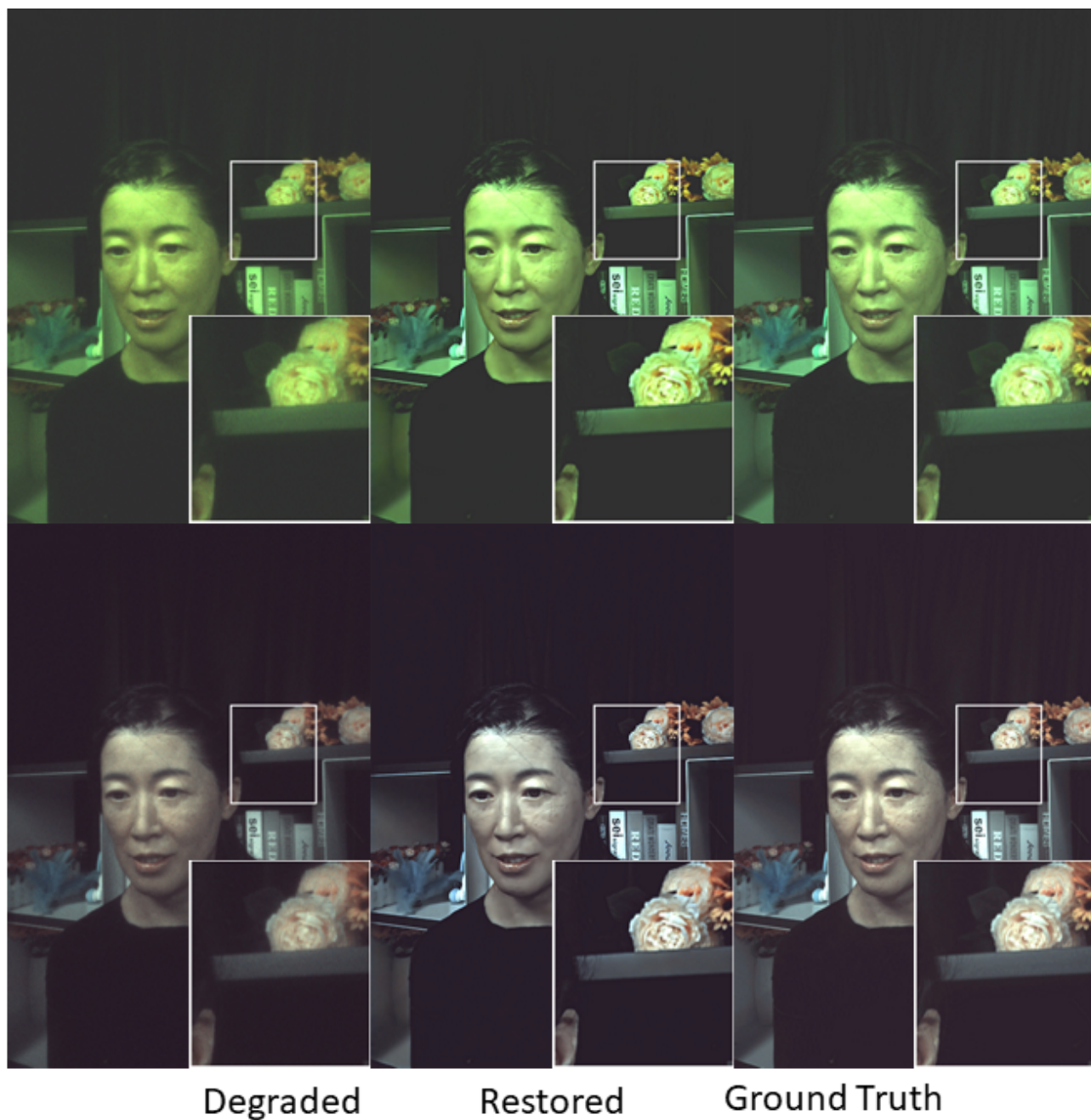


Figure S31. Some More Real World Data Results.



Figure S32. Some More Monitor Data Results.

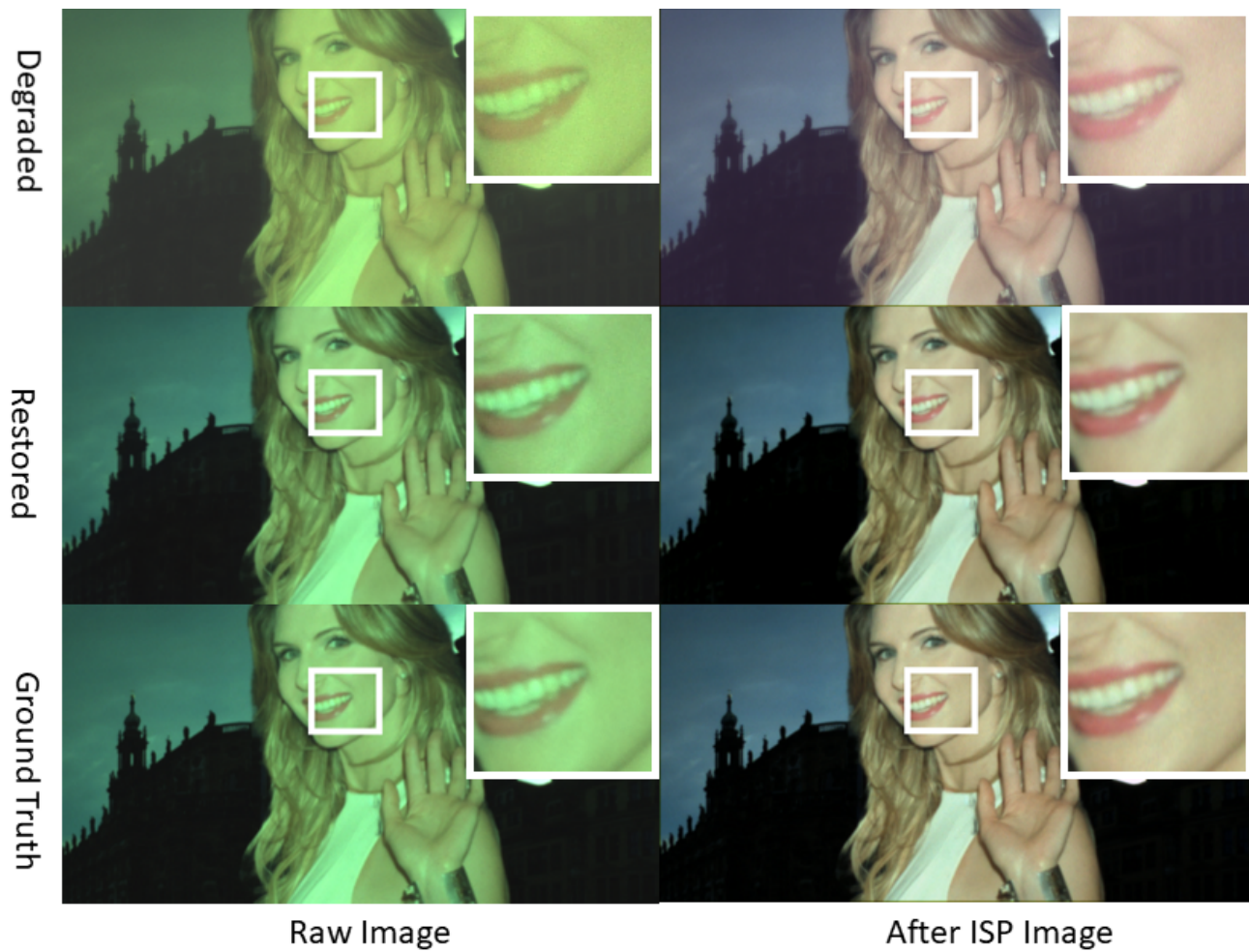


Figure S33. Some More Monitor Data Results.

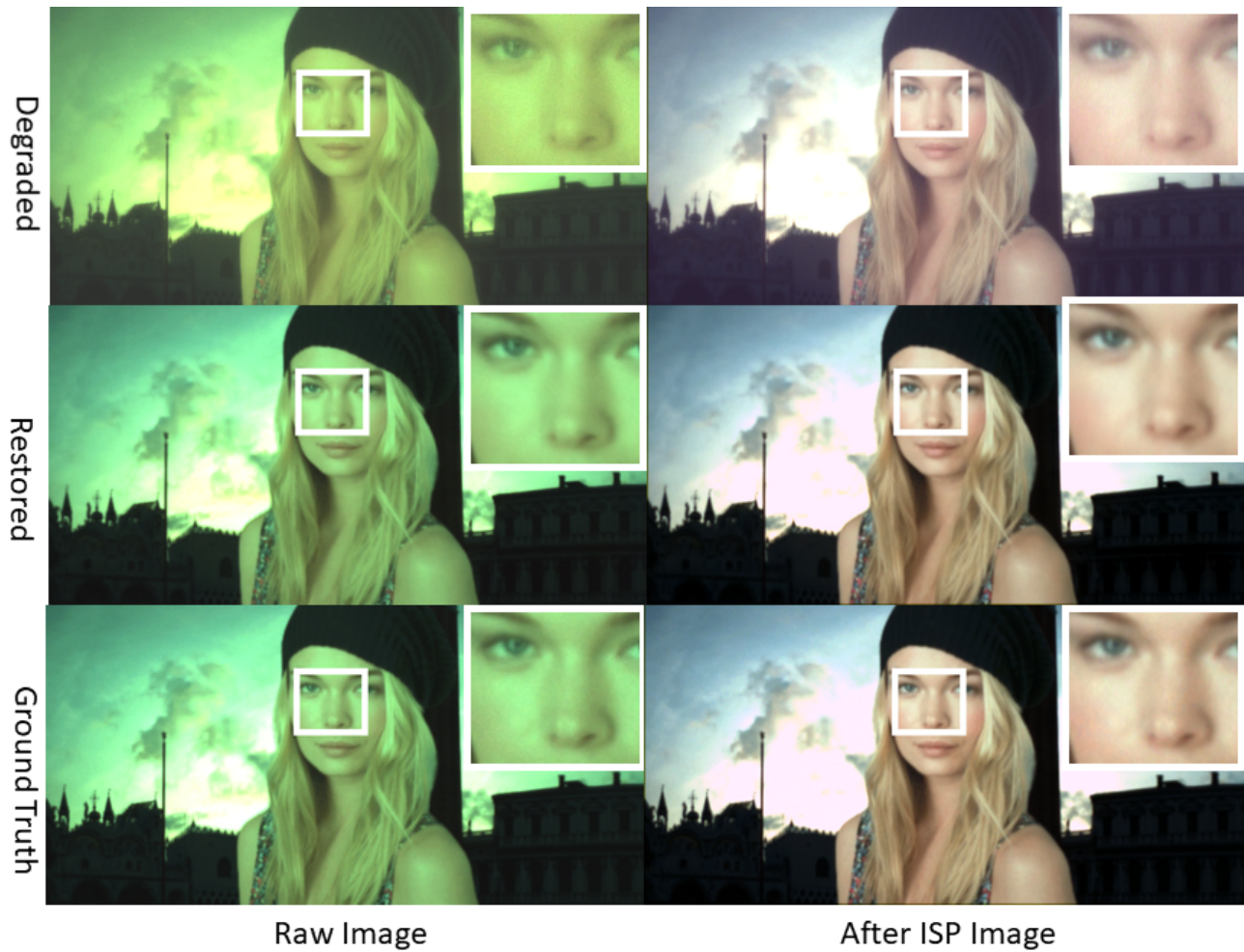


Figure S34. Some More Monitor Data Results.

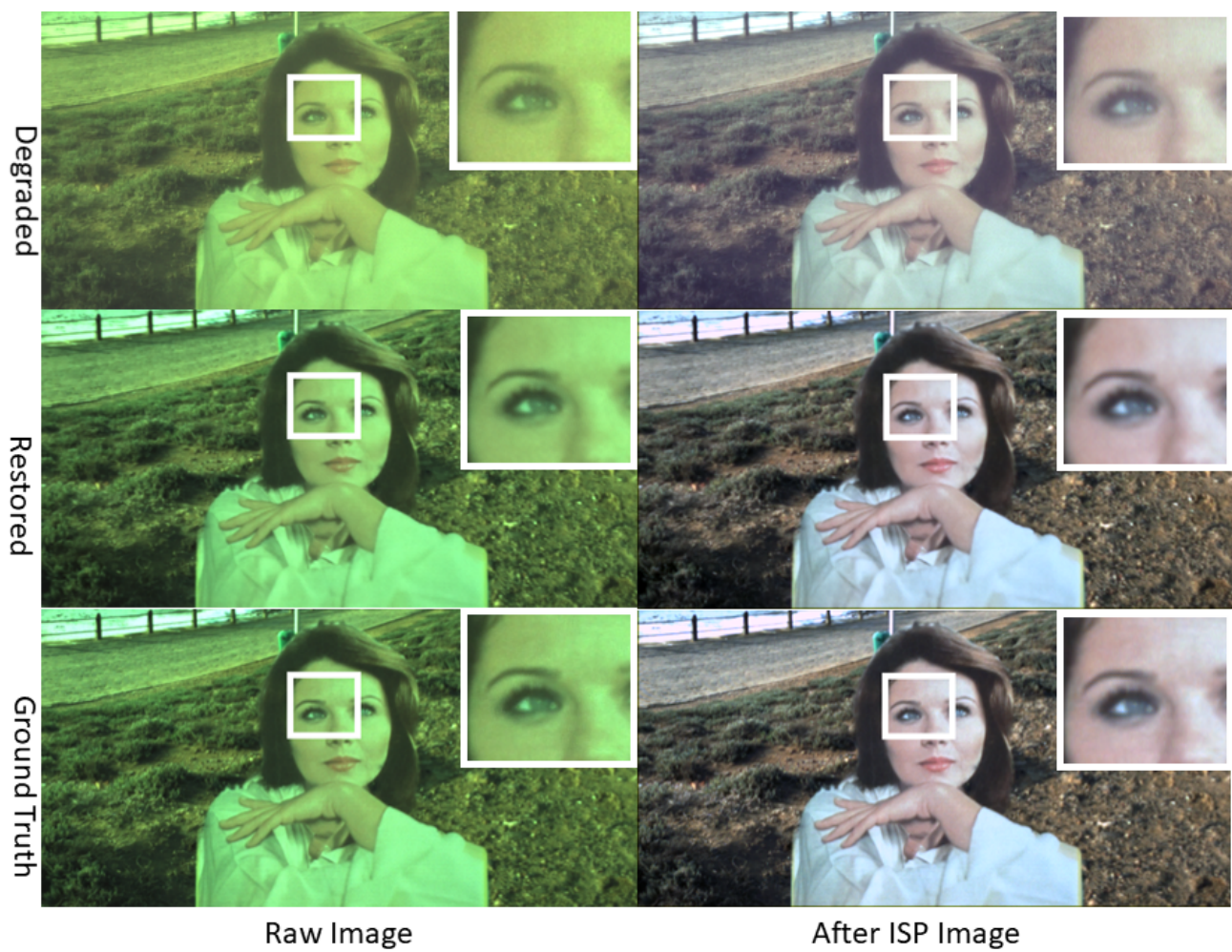


Figure S35. Some More Monitor Data Results.



Figure S36. Some More Monitor Data Results.